Oscillatory- and sector-zoned pyrochlore from carbonatites of the Kerimasi volcano, Gregory rift, Tanzania

Anatoly N. Zaitsev[1,2*], John Spratt[2], Alexander G. Shtukenberg[3], Andrei A. Zolotarev[4], Sergey N. Britvin[4], Sergey V. Petrov[5], Alina V. Kuptsova[6] and Anton V. Antonov[7]

[1]Department of Mineralogy, St. Petersburg State University, University Emb. 7/9, St. Petersburg, 199034, Russia; [2]Imaging and Analysis Centre, Department of Earth Sciences, The Natural History Museum, Cromwell Road, SW7 5BD, UK; [3]Department of Chemistry, New York University, 100 Washington Square East, New York, NY 10003, USA; [4]Department of Crystallography, St. Petersburg State University, University Emb. 7/9, St. Petersburg, 199034, Russia; [5]Department of Mineral Deposits, St. Petersburg State University, University Emb. 7/9, St. Petersburg, 199034, Russia; [6]Department of Regional Geology, St. Petersburg State University, University Emb. 7/9, St. Petersburg, 199034, Russia; [7]A.P. Karpinsky Russian Geological Research Institute, Sredny Pr. 74, St. Petersburg, 199106, Russia

*Author for correspondence: Anatoly N. Zaitsev. Email: a.zaitsev@spbu.ru

Prepublished Article

Abstract

The Quaternary carbonatite-nephelinite Kerimasi volcano is located within the Gregory rift in northern Tanzania. It is composed of nephelinitic and carbonatitic pyroclastic rocks, tuffs, tuff breccias and pyroclastic breccias, which contain blocks of different plutonic (predominantly ijolite) and volcanic (predominantly nephelinite) rocks including carbonatites. The plutonic and volcanic carbonatites both contain calcite as the major mineral with variable amounts of magnetite or magnesioferrite, apatite and forsterite. Carbonatites also contain accessory baddeleyite, kerimasite, pyrochlore and calzirtite. Zr and Nb minerals are rarely observed in rock samples, but are abundant in eluvial deposits of carbonatite tuff/pyroclastic breccias in the Loluni and Kisete craters. Pyrochlore, ideally $(CaNa)Nb_2O_6F$, occurs as octahedral and cubo-octahedral crystals up to 300 μm in size. Compositionally, pyrochlore from Loluni and Kisete

This is a 'preproof' accepted article for Mineralogical Magazine. This version may be subject to change during the production process.
DOI: 10.1180/mgm.2020.101

differs. The former is enriched in U (up to 19.4 wt.% UO_2), light REE (up to 8.3 wt.% $LREE_2O_3$), and Zr (up to 14.4 wt.% ZrO_2), and the latter contains elevated Ti (up to 7.3 wt.% TiO_2). All the crystals studied were crystalline, even those with high U content (a = 10.4152(1) Å for Loluni and a = 10.3763(1) Å for Kisete crystals). They show little or no subsolidus alteration nor low-temperature cation exchange (A site vacancy up to 1.5 % of the site), and are suitable for single-crystal X-ray diffraction analysis (R_1 = 0.0206 and 0.0140 for all independent reflections for Loluni and Kisete crystals respectively). Observed variations in the pyrochlore composition, particularly Zr content, from the Loluni and Kisete craters suggest crystallisation from compositionally different carbonatitic melts. The majority of studied pyrochlore crystals exhibit exceptionally preserved oscillatory- and sometimes sector-type zoning. The preferential incorporation of smaller and higher charged elements into more geometrically constrained sites on the growing surfaces explains the formation of the sector zoning. The oscillatory zoning can be rationalised by considering convectional instabilities of carbonatite magmas during their emplacement.

Keywords: pyrochlore, sector zoning, oscillatory zoning, carbonatite, Kerimasi volcano, Gregory Rift.

Prepublished Article

Introduction

Pyrochlore-group minerals, or simply pyrochlores (*sensu lato*), are complex Nb oxides that occur primarily as accessory minerals in diverse carbonatites, phoscorites and alkaline rocks (*e.g.*, Kapustin, 1980; Hogarth, 1989; Chakhmouradian and Williams, 2004). The crystal structure of pyrochlore-group minerals (simplified general formula of $A_2B_2O_6Z$) allows accommodation of Ca, Na, U, Th, Sr, Ba and rare earth elements (REE) as the principal cations in the *A* site, Ti, Ta, Zr and Fe as substituting cations for Nb in the *B* site, and F, OH group and O anions in the *Z* site (Hogarth, 1989). High compositional variability of pyrochlore is observed on a scale of a single carbonatite locality, a certain rock type, a single hand specimen and even a single crystal, suggesting a complex crystallisation and evolutionary history. Progressive changes in melt composition, typically in multi-stage carbonatite complexes, magma mixing and assimilation of early crystallised rocks can be responsible for the observed pyrochlore compositions (Chakhmouradian and Zaitsev, 1999; Hogarth *et al.*, 2000; Chakhmouradian and Williams, 2004; Zurevinski and Mitchell, 2004; Zaitsev *et al.*, 2012; Walter *et al.*, 2018). Late-stage hydrothermal alteration is particularly important and weathering of primary pyrochlore-group minerals leads to very intense cation substitution and cation leaching in the *A* site with the formation of hydrated and cation/anion-deficient minerals (Wall *et al.*, 1996; Nasraoui and Bilal, 2000; Melgarejo *et al.*, 2012). Another crucial alteration process is mineral decompression (metamictisation) due to decay of U and/or Th. As a result, primary unaltered and crystalline pyrochlore is extremely rare in carbonatitic rocks (Horarth and Horne, 1989). Pyrochlore-group minerals are also considered to be suitable for precision dating of carbonatitic rocks (Tappe *et al.*, 2009; Wetzel *et al.*, 2010; Belyatsky *et al.*, 2018). Last but not least, pyrochlore is highly important in Nb production with all major deposits related to carbonatitic rocks (Chakhmouradian *et al.*, 2015; Mitchell, 2015).

In this contribution we present and discuss compositional and structural data for pyrochlore from carbonatites associated with the Quaternary Kerimasi volcano located in the Gregory Rift in northern Tanzania. The young age of Kerimasi results in all studied crystals, even with high U content, being crystalline and showing little or no subsolidus alteration and low-temperature cation exchange.

Kerimasi volcano

Kerimasi is a large extinct stratovolcano with a diameter of about 14 km rising above the Gregory rift floor by approximately 1500 m. It is located *ca*. 12.5 km to the north of the currently active Oldoinyo Lengai carbonatite volcano (see Fig. 1 in Zaitsev *et al.*, 2010). Geological data and K-Ar dating of phlogopite from tuffs of Loolmurwak and Kisete craters suggest volcanic

Prepublished Article

activity between 1.2 and 0.4 Ma (Dawson and Powell, 1969; Macintyre *et al.*, 1974). Kerimasi is highly vegetated with limited outcrops in erosion gullies on the volcano slopes (Church, 1995) and in the upper parts of a debris avalanche deposit (Kervyn *et al.*, 2008; Delcamp *et al.*, 2016). The best outcrops with rocks considered to characterise Kerimasi are observed in the internal walls of Loluni, Kisete and Loolmurwak craters (Fig. 1) (Dawson and Powell, 1969; Hay, 1983).

The volcano consists of nephelinitic and carbonatitic pyroclastic rocks, tuffs and tuff breccias. No nephelinite and carbonatite lava flows are known at Kerimasi, and both rock types are observed as blocks in pyroclastic rocks only. Silicate and carbonate rocks at Kerimasi are represented by both plutonic and volcanic rocks (Dawson, 2008 and references herein). The silicate rocks include rare blocks of afrikandite (described as perovskite-bearing nepheline-melilite rock by Church (1995) and perovskite+magnetite+melilite-bearing clinopyroxene–nepheline rock by Guzmitc *et al.* (2012)), uncompahgrite (clinopyroxene-nepheline-melilite rocks, Church (1995)), clinopyroxenite and abundant blocks of texturally and compositionally diverse melteigite and ijolite (Church, 1995). The volcanic rocks include rare melilite nephelinite (Church, 1995; Zaitsev *et al.*, 2015) and abundant nephelinite and phonolitic nephelinite (Church, 1995). Melilite nephelinite is the most primitive volcanic rock at Kerimasi. However, the nephelinite is a relatively low magnesium rock (3.53 wt.% MgO, Mg# = 38.3); melilite, although classified as åkermanite, contains elevated amounts of Na (4.0-4.9 wt.% Na_2O) and Al (5.6-7.1 wt.% Al_2O_3) (Church, 1995; Zaitsev *et al.*, 2015) and therefore crystallised from an already evolved melt (Wiedenmann *et al.*, 2009, 2010).

Carbonatite tuffs, tuff breccias and pyroclastic breccias are widespread at Kerimasi and they contain blocks of both intrusive and effusive carbonatites. Outcrops with *in situ* carbonatites are extremely rare and they were described from the crater floor as a central plug (intrusive periclase-bearing calcite carbonatite, Mariano and Roeder, 1983), the lower eastern volcano flank (intrusive apatite-periclase-bearing calcite carbonatite, Church, 1995) and the eastern flank near the volcano summit (calcite carbonatite dyke, Church, 1995).

Samples of both intrusive and effusive carbonatites were collected from tuffs on the northern, eastern and southern slopes of the Kerimasi volcano, and from tuff breccias in Kisete, Loluni and Loolmurwak craters. Carbonatite samples from the Natural History Museum (London) collected by A. Church and M. Genge were also used in this study.

Blocks of intrusive carbonatite are holocrystalline with textures and mineralogy that are similar to early-stage, high-temperature magmatic carbonatites occurring worldwide (Kapustin, 1980; Chakhmoradian *et al.*, 2016 and references herein). Some of the carbonatites can be described as cumulate aggregates of calcite, apatite and magnetite or magnesioferrite; others can be termed as “banded” carbonatites with elongated calcite and apatite+magnetite segregations

Preprinted Article

between calcite crystals (probably correspond to a flow texture). All studied samples contain calcite as the major carbonate mineral; rare dolomite occurs as a secondary mineral along calcite grains boundaries. The carbonatites contain variable amounts of diverse minor and accessory minerals including apatite, magnetite, magnesioferrite, forsterite, spinel, monticellite, phlogopite, perovskite, calzirtite, pyrochlore, kerimasite and baddeleyite (Mariano and Roeder, 1983; Church, 1995; Dawson *et al.*, 1996; Reguir *et al.*, 2008; Zaitsev *et al.*, 2010; Guzmics *et al.*, 2011; Chakhmouradian *et al.*, 2017). Particularly interesting are carbonatites containing forsterite. The mineral is represented by two different crystal types, with rare oikocrysts (Fig. 2a) and common euhedral to subhedral crystals (Fig. 2b). The latter are partial to full pseudomorphs now.

The effusive carbonatites are also holocrystalline with pheno- and microphenocrysts of calcite as the major mineral in two texturally different carbonatite types (Hay, 1983; Mariano and Roeder, 1983; Church, 1995; Zaitsev, 2010). The first type contains tabular calcite pheno- and microphenocrysts which are single crystals and exhibit well developed zoning under cathodoluminescence. The second type of calcite occurs as abundant isometric or short tabular porous polycrystalline banded "pheno- and microphenocrysts" (termed as corduroy calcite by Church (1995)). Both calcite varieties are quite different in internal texture, composition and C-O isotope composition (Zaitsev, 2010; Zaitsev *et al.*, 2013).

Polycrystalline banded calcite crystals were interpreted as pseudomorphs after primary nyerereite, ideal formula $Na_2Ca(CO_3)_2$, (Hay, 1983) or as relicts of exsolved calcite lamellae from primary dolomite (Church, 1995). The absence of dolomite is explained by dolomite breakdown during fast magma ascent to the surface and late removal of breakdown products by alkaline-rich meteoric water. The occurrence of nyerereite in melt inclusions in magnesioferrite in carbonatite lava supports Hay's (1983) hypothesis that the formation of banded calcite may the result of complete nyerereite replacement, however, replacement of gregoryite, ideally $Na_2(CO_3)$, with exsolved nyerereite cannot be ruled out (Zaitsev, 2010). Texturally and mineralogically similar carbonatite lavas have been described from several other localities including Tinderet volcano (Deans and Roberts, 1984; Zaitsev *et al.*, 2013). Typical minor and accessory minerals in calcite carbonatite lavas are apatite, magnesioferrite or magnetite; rare accessories are pyrrhotite, forsterite, periclase, baddeleyite and pyrochlore (Hay, 1983; Mariano and Roeder, 1983; Church, 1995; Zaitsev *et al.*, 2008; Zaitsev, 2010).

Prepublished Article

Samples and methods

Two samples of eluvial deposits (about 10 kg each) on carbonatite tuff breccias were collected inside the Loluni and Kisete craters during 2005 field work and heavy mineral fractions were

separated by hand washing. Both samples contain abundant magnetite, perovskite and clinopyroxene of variable composition with minor baddeleyite, calzirtite, kerimasite, pyrochlore and cerianite (Zaitsev *et al.*, 2010, 2011).

Polished thin sections and blocks with mounted mineral grains were studied using a JEOL 5900LV scanning electron microscope equipped with an Oxford Instruments X-sight Si(Li) detector (The Natural History Museum, London) and a Hitachi S-3400N scanning electron microscope equipped with an Oxford Instruments X-Max 20 Energy Dispersive spectrometer (St. Petersburg State University). Electron-microprobe microanalyses of pyrochlore were obtained using wavelength-dispersive spectrometry (Cameca SX 50 microprobe, The Natural History Museum, London) with an accelerating voltage of 20 kV, beam current of 10 nA and electron-beam diameter of 1 μm (for detailed analytical conditions, including analysis of F, see Supplementary Table 1).

X-ray powder diffraction data were collected by the Gandolfi method (φ-ω rotation) using a Stoe IPDS II diffractometer (St. Petersburg State University) equipped with an Image Plate detector, Mo-*K*α source and graphite monochromator, operating at 50 kV, 40 mA, with a detector-to-crystal distance of 200 mm and an exposure time of 60 min.

For single-crystal study, pyrochlore crystals were placed on a STOE IPDS II diffractometer (Mo-Kα radiation, 50 kV, 40 mA) equipped with an Image Plate plane detector. The unit-cell parameters were refined by least square techniques. The structures have been solved by direct methods using the SHELX program package (Sheldrick, 2015) within the Olex2 shell (Dolomanov *et al*., 2009). Correction for absorption was introduced analytically with allowance for crystal shape. The final model included coordinates and anisotropic thermal parameters for all atoms.

Pyrochlore formulae were calculated on the assumption that the cation total in the *B* site is equal to 2. Nomenclature and classification of pyrochlore is based on Hogarth (1977) which is simple, clear and was used for many years in numerous publications related to pyrochlore-group minerals. Application of the current pyrochlore nomenclature and classification (Atencio *et al.,* 2010; Christy and Atencio, 2013) revealed several problems associated with the new mineral names (*e.g.*, Mitchell, 2015; Kasatkin *et al.*, 2020). For example, all analytical data obtained during this study correspond to an ideal pyrochlore formula $(CaNa)Nb_2O_6F$ (Table 1), which, ironically, is not considered in either Atencio *et al.* (2012) or Christy and Atencio (2013).

Statistical methods were applied to analyse oscillatory zoning in the pyrochlore crystals. Fractal dimensions of a strange attractor were calculated using a well-known correlation dimension method (Grassberger and Procaccia, 1984; Moon, 1987; Perugini *et al.*, 2005). A series of pseudo-phase spaces of different embedded dimensions $D_{emb} = 1, 2 \ldots 12$ was

Prepublished Article

constructed from a single "time series" (intensity of back-scattered electron image I as a function of spatial variable r – see Fig. 10 below), so that $I(D_{emb},r) = I(r + (D_{emb}-1)\Delta r)$. The value of shift Δr was chosen to be 10 points (pixels); variations of this value did not affect the result significantly. The correlation dimensions D were determined for all these pseudo-phase spaces. The higher embedded dimension used, the higher correlation dimension is obtained, however, starting from some D_{emb} the value of D stops changing, informing on the maximal dimension D_{max}. This value characterizes the fractal dimension of a strange attractor under consideration. Since the number of points in a profile is small (≤ 500), it was not obvious, if this approach can provide reliable results. Therefore, for the samples KS 24 and LL 445 measurements were also made for the same images with lower resolutions (161 instead of 285 and 265 instead of 500 points for the same profiles). The differences in D_{max} did not exceed 0.2 confirming applicability of our approach. The value of D_{max} contains information on the complexity of the system and the value $M = 1 + [D_{max}]$ (brackets denote truncation) represents the minimal number of ordinary differential equations that are necessary to reproduce the pattern observed (Moon, 1987).

Pyrochlore morphology, zoning and composition

Pyrochlore is an extremely rare mineral in the calcite carbonatite lavas, and relatively common, although accessory, in samples of intrusive calcite carbonatite. In thin section, pyrochlore occurs as euhedral to subhedral crystals up to 10 μm in diameter (with one crystal of 30 μm) and is typically observed in association with apatite or magnesioferrite/magnetite. A single pyrochlore crystal is present in a nyerereite inclusion in magnesioferrite in carbonatite lava (see Fig. 13 in Zaitsev *et al.*, 2008). In the heavy mineral fraction from carbonatite eluvial deposits within the Loluni and Kisete craters pyrochlore occurs as euhedral octahedral (common) to cubo-octahedral (rare) crystals up to 300 μm in size (Fig. 3). The cubo-octahedral crystals were observed in the sample from the Kisete crater only.

Back-scattered electron (BSE) images show that the majority of crystals studied are characterised by fine to coarse oscillatory (rhythmic) zoning, sometimes combined with sector zoning (Figs. 4, 5). A few crystals consist of, at least, two pyrochlore populations with compositionally different core and rims and both also display oscillatory zoning (Fig. 4c, Table 1). One crystal contains angular fragments of pyrochlore, which are mantled by homogeneous, but compositionally different pyrochlore (Fig. 4d, Table 1). Any features which can suggest late-stage alteration of pyrochlore (e.g. irregular, patchy zonation, veinlets) are extremely rare and observed in the outer part of the rim (Fig. 4b).

All crystals are compositionally inhomogeneous and characterised by large variations in the contents of major and minor elements; however, all data correspond to an ideal end-member

Prepublished Article

formula $(CaNa)Nb_2O_6F$ (Table 1). Although, there is a partial overlap of pyrochlore compositions from the Loluni and Kisete craters they are well separated on elemental X-Y plots (Fig. 6). Pyrochlore from Loluni is enriched in Zr, U and REE while pyrochlore from Kisete contains more Ti, Ca, Na and F. In total 150 spot analyses for 26 elements each were obtained from 22 pyrochlore crystals.

Nb is the dominant component of the *B*-site (38.1-67.7 wt.% Nb_2O_5, 1.22-1.89 apfu); Ti and Zr are present at elevated levels (from below detection limit (bdl) to 7.3 wt.% TiO_2, 0.33 apfu and to 14.4 wt.% ZrO_2, 0.50 apfu) and the Ta content is very low (bdl – 0.9 wt.% Ta_2O_5, 0.02 apfu). Na and Ca are dominant cations of the *A*-site (2.9-7.5 wt.% Na_2O, 0.36-0.90 apfu and 13.0-20.1 wt.% CaO, 0.94-1.41 apfu) and none from the other cations exceeds 20 % of total cations. Some of the pyrochlore crystals contain a considerable amount of U (up to 19.4 wt.% UO_2, 0.30 apfu) and can be termed as U-rich pyrochlore, while others are characterised by an elevated content of light rare earth elements (La-Sm) (up to 8.3 wt.% $LREE_2O_3$, 0.21 apfu) with Ce as the dominant element (Ce-rich pyrochlore). Minor components include Fe (up to 1.9 wt.% Fe_2O_3), Mg (up to 1.9 wt.% MgO) and Si (up to 2.3 wt.% SiO_2). Calculated mineral formulae show that *A*-site vacancy (up to 1.5 % of the site) is present in 29 analyses only (19 % of all analyses).

Individual crystals with oscillatory zoning show variations in all major and some minor elements including Ca, Na, Nb, Ti, Zr, U and REE. The largest absolute differences in neighboring zones correspond to Ca and Na (up to 0.14 apfu), whereas the maximum relative differences correspond to U and Ce (up to 50 %). Sector zoned crystals show enrichment of octahedral sectors in Na, U, Ti and Si and cubic sectors are enriched in Ca, Nb and rarely Zr (see below detailed discussion).

The characteristic feature of the pyrochlore from the Loluni crater is enrichment in Zr (Table 1, Fig. 6). It typically contains between 1.0 and 6.9 wt.% ZrO_2, and the angular cores in the crystal shown in Fig. 4e contain 12.3-14.4 wt.% ZrO_2. An exception is one crystal with well-developed oscillatory zoning (Fig. 4a), which contains little Zr (from bdl to 0.1 wt.% ZrO_2).

In strongly zoned crystals, with distinct core and rim (Fig. 4c), Zr is concentrated in the core (up to 4.6-6.9 wt.% ZrO_2); the element content decreases toward the outer part of the core (up to 1.1 wt.% ZrO_2) with the rim containing even less Zr (0.5-0.7 wt.% ZrO_2). The Zr-rich cores also contain significant U (up to 15.7 wt.% UO_2). As expected, Zr shows a negative correlation with Nb, as well as with Ca and F, and Zr positively correlates with U (Fig. 6).

Powder X-ray diffraction

X-ray diffraction data were obtained for five crystals with different compositions from the

Prepublished Article

Loluni and Kisete craters (Guteneva, 2012). The powder XRD patterns display well defined sharp lines which are indexed in the *Fd*-3*m* space group. The powder XRD data (*I*, *d* and *hkl*) for two crystals, one with the highest U and Zr content (LL 444) and another one with the lowest U and Zr (KS 21) are given in Supplementary Table 2. The unit-cell dimension *a* for the crystals from Loluni and Kisete are 10.4152(1) and 10.3763(1) Å, respectively.

Single-crystal X-ray diffraction analysis

The crystal structures were solved for eight samples from Loluni and Kisete (Guteneva, 2012) with the best sets of X-ray diffracted intensities collected from the pyrochlore crystals LL 441 and KS 23. The structure refinement yielded R_1 = 0.0206 and 0.0140 for all independent reflections for LL 441 and KS 23, respectively. The pyrochlore crystal structure is typical for pyrochlore-group minerals with the ideal formula $A_2B_2O_6Z_1$, *Fd*-3*m* space group, and based on an octahedral framework of corner-sharing BO_6 octahedra that form chains parallel to [110] direction with *A* cations and *Z* anions within the interframework space (Rouse *et al.*, 1998; Cámara *et al.*, 2004; Li *et al.*, 2016; Ivanyuk *et al.*, 2019)

The crystallographic data and parameters of refinement are given in Table 2; atomic coordinates, equivalent displacement parameters and site occupancies are given in Table 3; selected interatomic distances are given in Table 4. Anisotropic displacement parameters are given in Supplementary Table 3. Occupancies of the cation sites were calculated from the experimental site-scattering factors taking into account the empirical chemical composition. Occupancies of the cation sites were calculated from the experimental site-scattering factors taking into account the empirical chemical composition. The refined site occupancies for the *A*, *B* and *Z* sites are given in Table 3. For refinement of *B* site was used Nb scattering factors for both LL 441 and KS 23 crystals as well as F scattering factors was used for *Z* site. For refinement of *A* site was used mixed scattering factors Ca-U in the case of LL 441 and Ca-Na in the case of KS 23. These refined site occupancies were used to calculate the number of electrons per formula unit (epfu) for *A*, *B* and *Z* sites, *i.e.* refined site scattering factors (Table 3). At the same time, taking into account the data of chemical analysis, the final occupancies for the *A*, *B* and *Z* sites were calculated. In this case, again were calculated the number of electrons per formula unit (epfu) for *A*, *B* and *Z* sites, *i.e.* calculated site scattering factors (Table 3). We distributed the cations by sites according to the distribution that indicated in Table 1: *A*-site: Ca, Na, U, REE, Mn, Sr; *B*-site: Nb, Zr, Ti, Si, Fe, Mg, Al. The O/OH/F ratio in *O* and *Z* sites is calculated from the charge balance of formulas and amount of F. It should be noted that the values of refined site scattering and calculated site scattering factors are in good agreement,

Prepublished Article

which indicates the reliability of our proposed model of the occupancies of the *A*, *B* and *Z* sites discussed below.

The *A* (16d) site has 8-fold coordination with 6 O and 2 *Z* anions with the mean <*A*-O,*Z*> bond length of 2.534 Å and 2.532 Å for LL 441 and KS 23, respectively (Table 4). The *A* site in both crystals is predominantly occupied by Ca and, to a lesser extent, by Na. However, the differences in Ca and Na cannot account for significant observed differences in the occupancy of the *A* site. The refined site-scattering factors for the *A* site are 25.0 and 17.1 electron per formula unit (epfu) for LL 441 and KS 23, respectively (Table 3). This difference is explained by the presence of a significant amount of REE and U in sample LL 441 (Table 1). On the other hand, sample KS 23 is depleted in these elements compared to LL 441, and the *A* site is almost completely occupied by Ca and Na (Table 1). The full occupancy of *A* site can be given as: $(Ca_{0.515}Na_{0.325}U_{0.08}Ce_{0.06}La_{0.01}Nd_{0.01}Pr_{0.005}Mn_{0.005}Sr_{0.005}Y_{0.005})$ for the LL 441 sample and $(Ca_{0.58}Na_{0.39}U_{0.015}Sr_{0.01})$ for the KS 23 sample, respectively.

The *B* (16c) site is octahedrally coordinated by 6 O with the mean <*B*-O> bond length of 1.988 Å and 1.975 Å for LL 441 and KS 23, respectively (Table 4). The octahedral *B* site for both samples is predominantly occupied by Nb atoms. The refined site-scattering factors for the *B* site are 38.13 and 37.72 epfu for LL 441 and KS 23, respectively (Table 3). However, despite the similarity of calculated epfu values, this site is occupied differently. The LL 441 sample is characterized by a significant amount of Zr, Fe and Mg, with an almost complete absence of Ti, while KS 23 contains a significant amount of Ti and practically no Zr. The full occupancy of the *B* site can be given as: $(Nb_{0.865}Zr_{0.06}Mg_{0.04}Fe_{0.035}Al_{0.005})$ for the LL 441 sample and $(Nb_{0.835}Ti_{0.11}Si_{0.03}Fe_{0.02}Zr_{0.005})$ for the KS 23 sample.

The O (48f) site is occupied by oxygen with minor (OH) group in KS 23 crystal. The *Z* (8b) site is occupied by F and O for LL 441 sample with occupancy $(F_{0.54}O_{0.46})$ and by F and OH in the case of KS 23 sample with occupancy $F_{0.90}OH_{0.10}$ (Table 3). The O/OH/F ratio in O and *Z* sites was calculated from the charge balance arguments and F content which was determined by electron microprobe analysis.

In summary, the crystal chemical formulae of the pyrochlore can be written as $(Ca_{1.03}Na_{0.65}U_{0.16}Ce_{0.12}La_{0.02}Nd_{0.02}Pr_{0.01}Mn_{0.01}Sr_{0.01}Y_{0.01})_{\sum 2.03}(Nb_{1.73}Zr_{0.12}Mg_{0.08}Fe_{0.07}Al_{0.01})_{\sum 2.00}O_6(F_{0.54}O_{0.46})_{\sum 1.00}$ for the LL 441 crystal and $(Ca_{1.16}Na_{0.78}U_{0.03}Sr_{0.02})_{\sum 1.99}(Nb_{1.67}Ti_{0.22}Si_{0.06}Fe_{0.04}Zr_{0.01})_{\sum 2.00}(O_{5.89}OH_{0.11})_{\sum 6.00}(F_{0.90}OH_{0.10})_{\sum 1.00}$ for the KS 23 crystal. Both crystal chemical formulae are in good agreement with the empirical formulae (Table 1).

Discussion

Prepublished Article

Compositional variations

Pyrochlore-group minerals in carbonatites are recognised as important tracers of geochemical evolution of carbonatite melts, they are key indicators of different subsolidus processes (e.g. recrystallization, hydrothermal alteration, weathering) and help in an understanding of the processes related to carbonatite formation (fractional crystallisation, liquid immiscibility and magma mixing) as well as relationships with associated silicate rocks (*e.g*., Chakhmouradian and Zaitsev, 1999; Hogarth *et al*., 2000; Chakhmouradian and Williams, 2004; Zurevinski and Mitchell, 2004; Lee *et al*., 2006; Zaitsev *et al*., 2012; Walter *et al*., 2018). The major problem in pyrochlore studies seems to be an "old" emplacement age for the majority of carbonatites. Decay of U and Th, common elements in early crystallised pyrochlore, and low temperature hydrothermal activity lead to the destruction of crystal structure and significant changes in mineral composition, particularly in the *A* site. Due to this, primary textures and compositions are rarely observed in pyrochlore (Hogarth *et al*., 2000), but they can be relatively common in pyrochlore from "young" carbonatites, *e.g*., from the Kaiserstuhl plutono-volcanic complex (Walter *et al*., 2018), Tinderet volcano (Zaitsev *et al*., 2013), Camile dyke at São Vicente island (Cape Verde) (Hodgson and Le Bas, 1992) and Fort Portal volcano (Hogarth and Horne, 1989). All these processes, which have a strong influence on changes of pyrochlore texture and composition, are lacking at Kerimasi where pyrochlore is crystalline even with 19.4 wt.% UO_2, exhibits well-developed compositional zoning and has little or no sign of hydrothermal alteration. Lack of hydrothermal overprint could be related to volatile loss during volcanic activity and/or magma rapid ascent and eruption without long-time storage in crustal intermediate chamber(s) under closed-system conditions. Results of detailed study of pyrochlore from the Kaiserstuhl volcanic complex show that hydrothermal alteration could be a common phenomenon in carbonatites crystallised from an evolved melt and also related to the geometry and size of carbonatite bodies (Walter *et al.*, 2018).

Prepublished Article

Compositionally, pyrochlore from Kerimasi differs from pyrochlore-group minerals from many other localities in that it lacks an early-crystallised U-Ta-rich pyrochlore (uranopyrochlore) (*e.g*., Chakhmouradian and Zaitsev, 1999; Subbotin and Subbotina, 2000; Chakhmouradian and Williams, 2004; Lee *et al*., 2006; Zaitsev *et al*., 2012; Viladkar *et al.*, 2017; Walter *et al*., 2018). Although the U content can be as high as 19.4 wt.% UO_2, the concentration of Ta is extremely low (≤0.9 wt.% Ta_2O_5 only). Instead of Ta, the pyrochlore with high U contains elevated levels of Zr and rarely Ti (Table 1, Fig. 6).

Zr-rich pyrochlore-group minerals are not common for carbonatites; typically ZrO_2 in pyrochlore does not exceed 4-5 wt.% (*e.g.*, Hogarth et al., 2000; Chakhmouradian and Williams, 2004; Melgarejo *et al.*, 2012; Zaitsev *et al*., 2012, 2014). Examples with much higher Zr

concentration in pyrochlore-group minerals are rare and include carbonatites from the Oka complex (up to 16.3 wt.% ZrO_2, Zurevinski and Mitchell, 2004), Kaiserstuhl (up to 12.5 wt.%, Walter *et al.*, 2018), Kovdor (up to 12.4 wt.%, authors unpublished data), Camile dyke at São Vicente island (up to 10.3 wt.%, Hodgson and Le Bas, 1992) and Vuoriyarvi (up to 8.7 wt.%, Chakhmouradian and Williams, 2004). Zr-rich pyrochlore also occurs in Guaniamo kimberlites (up to 23.7 wt.% ZrO_2, Sharygin *et al*., 2009) and syenitic ejecta in pyroclastic rocks of the Sabatini volcano (up to 8.4 wt.%, Caprilli et al., 2006). High Zr content in pyrochlore, particularly in publications where wet chemical analysis of bulk samples was used, could be related to the presence of baddeleyite inclusions in pyrochlore (Yaroshevskii and Bagdasarov, 2008). Indeed, abundant fine baddeleyite needles are present in pyrochlore, *e.g*., in Kovdor carbonatites (Fig. 7a) and their appearance can result from exsolution or simultaneous mineral growth. At Kerimasi the pyrochlore does not contain exsolved baddeleyite, although baddeleyite was observed as rare relics in pyrochlore cores (Fig. 7b).

Zr is obviously present in the *B* site of the crystals studied here; pyrochlore from the Loluni crater exhibits a negative correlation with Nb, but no positive or negative correlation with Ti is observed (Fig. 6). In addition, the analysed crystals from Loluni have an anion excess in the *Z* site assuming the site occupancy by (OH) in addition to F for the charge balance; totals for F + (OH) vary between 1.04 and 1.50. This could be an indication of the presence of O instead of (OH) at the *Z* site as suggested by Sharygin *et al.* (2009). Simplified substitution, involving *A*, *B* and *Z* sites, can be suggested as $U^{4+} + Zr^{4+} + O^{2-} \rightarrow Ca^{2+} + Nb^{5+} + F^-$.

The presence of O at the *Z* site (when the *B* site is predominantly occupied by pentavalent cations) will entirely depend on *A* cations. Thus, increasing the amount of U^{4+} and REE^{3+} would require increasing O^{2-} at the *Z* site to maintain the charge balance. This scenario is realised for pyrochlore crystals from the Loluni crater.

Excluding synthetic oxy-compounds with a pyrochlore-type structure, well-studied natural pyrochlore-group minerals with O at the *Z* site are rare. Examples are stibiobetafite from pegmatite, Vežná serpentinite (Černý *et al.*, 1979), uranbetafite from foid-bearing syenite ejectum in pyroclastic rock, Vico volcanic complex (Cámara *et al.*, 2004), pyrochlore from calcite-magnetite-forsterite phoscorite, Kovdor plutonic complex (Ivanyuk *et al.*, 2018) and oxybismutomicrolite from granitic pegmatite, Malkhan (Kasatkin *et al.*, 2020) where compositional and single-crystals X-ray diffraction data suggest O dominance in the *Z* site.

The pyrochlore from the Loluni crater is remarkably similar to that of the Camile dyke at São Vicente island (Hodgson and Le Bas, 1992). The latter occurs as cubic and cubo-octahedral sector zoned crystals; it is rich in U (up to 16.8 wt.% UO_2), Zr (up to 10.3 wt.% ZrO_2) and poor in Ta (up to 0.4 wt.% Ta_2O_5). Moreover, it contains Si (up to 2.4 wt.% SiO_2) in an octahedron

Prepublished Article

growth sector (see below).

High concentration of Zr is a characteristic feature of the Kerimasi intrusive carbonatites, which contain baddeleyite, calzirtite and kerimasite – all Zr minerals *sensu stricto* (Church, 1995; Zaitsev *et al.*, 2010). Zirconolite was also described by Church (1995) but was not found in this study. Unfortunately, the relationships between these minerals (*e.g.*, succession of their crystallisation) are poorly known. Limited observations show that baddeleyite was the first mineral to crystallise and was replaced and overgrown by kerimasite (see Fig. 2d in Zaitsev *et al*., 2010) or pyrochlore (Fig. 7b). Calzirtite crystals always occur separately from other Zr minerals.

Another compositional feature of the Kerimasi pyrochlore is the variable content of Si (Table 1). The pyrochlore from Loluni contains very low Si that varies from bdl to 0.16 wt.% SiO_2; in contrast, pyrochlore from Kisete is enriched in Si with a maximum value of 2.28 wt.% SiO_2. The element is present in crystals with sector zoning (Table 1, Fig. 5) and it is concentrated in octahedral growth sectors (0.24-2.28 wt.%, with average 0.86 and 1σ = 0.46 wt.%); cubic growth sectors are depleted in Si and contains from bdl to 0.17 wt.% SiO_2 only (average 0.06 with 1σ = 0.04 wt.%).

Si is still an enigmatic component of pyrochlore-group minerals, generally its concentration in primary, unaltered minerals is very low, but can reach several wt.% in highly altered crystals, *e.g.*, up to 4.7 wt.% SiO_2 in pyrochlore from the Khibina carbonatites (Zaitsev *et al*., 2012). Other examples of Si-enriched pyrochlore-group minerals include pyrochlore from the Meech Lake glimmerite (Hogarth *et al*., 2000), diverse alkaline rocks from Lovozero, Khibina, Vishnevye Mountains and other localities (Chakhmouradian and Mitchell, 2002). Single-crystal X-ray diffraction analysis and transmission electron microscopy suggest that Si can be present "in an amorphous or dispersed state" (Voloshin *et al*., 1989, p. 19) or "only a fraction (~30–50%) of the Si… is incorporated within the structure… The remaining 50–70%… is incorporated in the radiation-damaged portions of pyrochlore" (Bonazzi *et al*., 2006, p. 794). In our case, the crystals crystallinity, internal zoning, composition and lack of subsolidus alteration (Table 1, Fig. 5) suggest that Si is present in the *B* site of the Kisete pyrochlore.

Sector zoning

The pyrochlore crystals from Kisete exhibiting both {100} and {111} growth sectors demonstrate sector zoning in BSE intensity (Fig. 5), *i.e*. variations in chemical composition. Since these crystals possess pronounced concentric zoning, comparison of different sectors was obtained for the chronologically equivalent growth zones. The compositional data of corresponding pairs of points is listed in Table 1, shown on Supplementary Figure 1 and the

Prepublished Article

intersectorial differences for the most significant elements are listed in Table 5 along with the data from São Vicente (Hodgson and Le Bas, 1992), to our knowledge the only paper considering pyrochlore sector zoning.

Table 5 shows that growth sectors of octahedron are always enriched in Ti, Na, U, Fe and Si, whereas growth sectors of cube are enriched in Nb (with one exception) and Ca. Due to the small concentrations no definitive conclusion can be deducted for other elements. One can expect that K is enriched in the {111} growth sectors in the Kisete crystals and in the {100} growth sectors in crystals from São Vicente (Hodgson and Le Bas, 1992), however, there is too little information to be confident. Likewise the {100} growth sectors in crystals from São Vicente seem to be enriched in La and depleted in Pb (Hodgson and Le Bas, 1992). The intersectorial differences $\Delta x = x_{\{111\}} - x_{\{100\}}$ for the major elements (Na, Ca, U, Nb, Ti) can be as high as 0.15; the range of Δx variations is similar for the elements occupying the *A* and *B* sites. The values Δx for the same element vary significantly over individual crystals and zones within one crystal. There is a weak positive correlation between the difference Δx and the average concentration $x_{av} = (x_{\{111\}} + x_{\{100\}})/2$.

Several main mechanisms were proposed to explain formation of sector zoning: (1) Differences in growth rates of non-equivalent crystal faces define a different diffusion supply of components to the faces (Albarede and Bottinga, 1972; Tiller and Ahn, 1980; Tiller, 1986). This mechanism requires significant differences in growth rates of corresponding faces (Shtukenberg *et al*., 2009) and, therefore, is inapplicable for isometric pyrochlore crystals, for which cube and octahedron can coexist in the crystal habit only if their relative growth rates differ by a factor of less than $\sqrt{3}$ (Fig. 5). (2) Differences in growth rates of non-equivalent crystal faces define different attachment of components to the faces (Tauson, 2005; Shtukenberg *et al*., 2009). This mechanism is plausible, and it typically accompanies mechanism (3) but it cannot be verified owing to the lack of information on the growth rate dependence of the distribution coefficient. (3) An additional plausible explanation is the selective adsorption of components to the face due to the differences in atomic structure of crystallographically non-equivalent crystal surfaces (Hollister, 1970; Hollister and Gancarz, 1971; Dowty, 1976; Chakhmouradian *et al*., 2007). This mechanism requires different atomic arrangements of proto-sites on different growth faces, a feature that was observed for a series of compounds with sector zoning, *e.g.*, staurolite (Hollister, 1970), clinopyroxene (Hollister and Gancarz, 1971), monazite (Cressey *et al.*, 1999), perovskite (Chakhmouradian *et al.*, 2007) among others. Below we explore the latter hypothesis in more detail.

We assume that pyrochlore crystal faces {*hkl*} grow by elementary steps moving along a smooth face and having the heights of interplanar distance d_{hkl} corrected for the presence of

Prepublished Article

translation normal to the crystal face. Although incorporation occurs at kink sites on growth steps, it is sufficient to analyze the geometrical non-equivalence of sites with respect to the growth face. Indeed, any face is formed by steps of several orientations and moving in different directions. This should provide strong sub-sector or intrasector zoning (Paquette and Reeder, 1990; Rakovan and Reeder, 1994), which is infrequent and, if observed, is typically much weaker than sector zoning. The most probable reason for this apparent contradiction is the diffusion relaxation, which is fast in the sub-surface layers and which transforms the distribution of atoms corresponding to the growth steps on the face to that corresponding to the face itself (Chernov, 1984; Shtukenberg *et al*., 2005). Additionally, in most cases predictions outlined for the faces remain valid for the steps on these faces.

At the growing face, some sites are geometrically more constrained than the others, allowing preferential incorporation of isomorphic ions into specific sites located on different growth faces and forming a basis for the sector zoning. Dowty (1976) has suggested that smaller and higher charged ions will easily and strongly adsorb into any sites, while larger and lower charged ions will less likely adsorb into more geometrically constrained sites. Thus, more geometrically constrained sites will be preferably occupied by smaller and higher charged ions.

Fig. 8 shows the atomic arrangement in the surface layer on the {111} and {100} faces. On the {111} face there are two types of layers, which create two different arrangements for *A* sites. The first type (Fig. 8a) features six *A*-O bonds that are located in the surface layer and two reminding *A*-F bonds are directed inward and outward of the layer, respectively. The second type (Fig. 8b) is characterized by four *A*-O and two *A*-F bonds lying in the surface layer with two reminding *A*-O bonds directed inward and outward of the layer, respectively. The atomic surrounding of all *A* sites on the {100} growth face (Fig. 8c) is very similar to the latter case. Since *A*-O bonds ($d_{A\text{-O}}$ = 2.57 Å) are slightly weaker than *A*-F bonds ($d_{A\text{-F}}$ = 2.25 Å) *A* sites on the {100} faces are slightly more under-bonded compared with *A* sites on the {111} ones meaning that {100} growth sectors should be preferentially occupied by smaller and higher charged cations in *A* site. This is correct for Na^{+} (1.32 Å) and Ca^{2+} (1.26 Å), but opposite for U^{4+} (1.14 Å) (here and below ionic radii from Shannon (1976) are given in parentheses.)

The *B* sites are located inside growth layers for both {100} and {111} growth surfaces and their first coordination spheres are completed. However, in cases shown in Fig. 8b,c three *B*-O bonds involve oxygen atoms on the outer surface of the growth layer, while for one layer on the {111} face (Fig. 4a) there is only one such oxygen. Since surface oxygens can be removed easier, *B* sites on the {111} growth faces are under stronger geometrical constraints and should be considered as less under-bonded, meaning that {111} growth sectors should be preferentially occupied by smaller and higher charged *B* cations. Indeed, the smaller Ti^{4+} (0.75 Å), and Si^{4+}

Prepublished Article

(0.54 Å) prefer the {111} growth sectors, while the larger Nb^{5+} (0.78 Å) the {100} ones. The charge difference between Nb^{5+} *vs*. Ti^{4+} is apparently not significant enough to counteract the difference in ionic radii. Low charged and large Fe^{3+} (0.79 Å), however, also prefers the {111} growth sectors that may reflect preferential incorporation of Fe to be controlled by the charge compensation mechanisms rather than the geometrical constraints (Chakhmouradian *et al*., 2007).

Perovskite-group minerals are very similar to pyrochlore-group minerals. They have comparable composition ABO_3 (*A* = Ca, Na, Sr, LREE, U…; *B* = Ti, Nb, Fe…), form cubic crystal structures with BO_6 octahedra linked by corners and with the cavities filled by *A* ions in 12-fold coordination and their crystal shapes are dominated by the cube and octahedron. Therefore, it is worth comparing sector zoning in these minerals. The sector zoning in perovskite was analyzed in detail (Chakhmouradian *et al*., 2007) and it was found that the {100} sectors were enriched in K, Ce, Ti, Sr, Ba, Y, Th, U, Fe, Si and Zr with respect to the {111} sectors, which showed higher levels of Ta, Ca, Nb, and sometimes Na. Thus, the elements that reveal strong and consistent sector zoning in both minerals (Ca, Nb, U, Si, Fe), have the opposite preferable incorporation into {100} and {111} growth sectors. The opposite preferable incorporation is well corroborated with the opposite distribution of more and less geometrically constrained sites on the corresponding growth faces (Fig. 9).

The simple geometrical analysis correctly predicts sector zoning in both, pyrochlore and perovskite, and highlights the importance of structural control in sector zoning formation. The correspondence is not perfect, however. In pyrochlore, the behavior of U does not obey Dowty's hypothesis and some minor elements including K, Pb, Ce, La and Zr do not show a consistent sector zoning pattern. One possible reason for the discrepancy is the complex nature of element substitutions in pyrochlore that makes the *A* and *B* sites interdependent on one another. While the major components follow the substitution mechanism $Na^{+} + Nb^{5+} \leftrightarrow Ca^{2+} + Ti^{4+}$, the other components like U^{4+} or REE^{3+} require different substitution mechanisms that may only partially comply with the geometrical constraints. Additionally, the analysis above does not consider the effect of growth kinetics on distribution coefficients and sector zoning (mechanism (2)) that may be significant.

Oscillatory zoning

Oscillatory zoning is more common than sector zoning in pyrochlore crystals (Hogarth *et al*., 2000; Zurevinski and Mitchell, 2004; Lee *et al*., 2006; Sharygin *et al*., 2009; Walter *et al*., 2018; Mitchell *et al*., 2020). Crystals from both Loluni and Kisete are also characterized by a distinct μm-scale oscillatory zoning (Figs. 4, 5, 7, 10). The largest absolute differences between

Prepublished Article

neighboring zones correspond to Ca and Na (up to 0.14 apfu), whereas the maximal relative differences correspond to U and Ce (up to 50 %). Concentrations of U, Ce, Ca, Fe, Mg show sympathetic relations with the brightness of BSE images, whereas Nb and Na exhibit an antipathetic relation (Fig. 11). Correlation between individual elements is present but not very strong suggesting different evolution trends for different elements. Our new and previously published data (Hogarth *et al*., 2000; Subbotin, Subbotina, 2000; Zurevinski and Mitchell, 2004; Walter *et al*., 2018; Mitchell *et al*., 2020; Lee *et al*., 2006) have revealed some common features of pyrochlore oscillatory zoning. The zoning is variable: it can be found throughout the whole crystal or in limited regions; there are also crystals without oscillatory zoning. The oscillatory zoning is observed in crystals of different compositions. Even within one sample it is possible to find crystals of different composition and zoning (Zurevinski and Mitchell, 2004). The thickness of zones varies from few μm up to hundreds of μm. The boundaries between individual zones are sharp and compositional variations within each zone are slight (due to the data averaging normal to the growth direction profiles in Fig. 10 are even slightly smoother than in reality). The zoning pattern is the same within any growth sector and in different growth sectors of the same crystal.

A number of mechanisms can form oscillatory zoning in minerals (some of these are reviewed by Shore and Fowler (1996)), and the applicability of these to pyrochlore is discussed below.

Growth rate variations can affect distribution coefficients and crystal composition, however, because of very large concentration differences between the neighboring zones such a mechanism would require non-realistic growth rate variations. Other external factors such as sudden temperature variations, pressure release, and loss of volatile components due to the system opening should be ruled out because all these catastrophic events are followed by a gradual relaxation of the system that should result in asymmetric zoning profiles. In reality, compositional changes between different zones are typically sharp without asymmetrical gradation (Figs. 4, 5, 7, 10).

Periodic magma injections with subsequent magma mixing could be another reason for formation of oscillatory zoning in mineral crystals. Early-stage, high-temperature carbonatites typically form magmatic sheet intrusions, dykes and dykelets, with variable thickness-to-length scale. The low viscosity of a carbonatite melt (Treiman, 1989) suggests a turbulent flow of magma and the formation of convection cells in dykes. Therefore, unlike basalt and rhyolite magmas (Perugini *et al*., 2003) a long-term mixing process during carbonatite formation is impossible and cannot be responsible for the appearance of oscillatory zoning in pyrochlore (in contrast to, *e.g.*, plagioclase (Perugini *et al*., 2005)).

Prepublished Article

Diffusion-attachment instabilities at the growth front (L'Heureux, Fowler, 1994; L'Heureux, Katsev, 2006; Kalischewski *et al*., 2007) can also lead to the compositional oscillations. However, any such mechanism typically produces oscillations in a narrow range of chemical composition and growth conditions, while oscillatory zoning in pyrochlore features crystals of very different compositions and compositional variations.

Micromorphological instabilities of the growing face (Shtukenberg and Punin, 2011) are not applicable here, because the zoning patterns are very similar in different parts of the same growth sector and in different growth sectors of the same crystal. Moreover, compositional variations between neighboring zones of the same crystal are too large to be produced by this mechanism.

Thus, external oscillations, diffusion-attachment instabilities, and instabilities of crystal growth cannot significantly contribute to oscillatory zoning in pyrochlore. All the observed features, however, can be explained via convectional instabilities in magma (Fig. 12a). Indeed, magma in the chamber can be chemically stratified. The pyrochlore crystals are small (usually < 1 mm, our crystals < 0.3 mm) and should be influenced by flows and convection currents with no or slight gravitational settling (Treiman, 1989). Any particular crystal can follow convection currents for a long time. During this time it would be in contact with the same melt and produces a chemically homogeneous zone. However, due to hydrodynamic instabilities the crystal can migrate into another convection circle or get into stagnant melt between neighboring currents or near the dyke wall. At this moment the melt composition changes abruptly and a zone of another composition starts forming. The crystal can then migrate either back to the original convection current or into some other area of the growth chamber. As a result, crystals nucleated in the same area can be found in different parts of the chamber. Conversely, crystals with different growth histories can come to the same area at the final stage of crystallization. This model can explain the occurrence of chemically different crystals (Zurevinski and Mitchell, 2004) or crystals with and without oscillatory zoning (Hodgson and Le Bas, 1992) in samples located not far from one another (spaced less than 1 meter).

Mass transfer in a dyke is similar to mass transfer in a vertical flat layer heated from the bottom. Experimental modeling of hydrothermal crystal growth in such a layer (Popov *et al*., 2006) has confirmed the intuitive arguments formulated above. It was observed that for some time solution circulated within stratified convective currents. Then, suddenly the liquid was exchanged between upper and lower currents. This event was followed by another period of more organized flow within newly established convective cells.

Statistical analysis of oscillatory zoning (Table 6) has determined that the values of fractal dimension of strange attractor D_{max} for all analyzed crystals are essentially the same and

Prepublished Article

slightly smaller than 3 (except for one case where D_{max} = 3.8). This range corresponds to chaotic dynamics of the system, neither deterministic (D_{max} = 1), nor random (D_{max} is high and approaches infinity). The values are close to one another suggesting a similar origin of oscillatory zoning in all crystals studied, including those from the Fen complex, Norway (Hogarth *et al*., 2000) and from Kovdor (author's unpublished data). This result is not surprising, since visually oscillatory zoning in pyrochlore of differing compositions and from different localities looks very similar, see Figs. 4, 5, 7 and also BSE images in Hogarth *et al*. (2000), Subbotin and Subbotina (2000), Zurevinski and Mitchell (2004), Walter *et al*. (2018). Since in the most cases D_{max} < 3, formation of oscillatory zoning is supposed to be controlled by three ordinary differential equations (Moon, 1987). This hypothesis is consistent with the fact that Rayleigh–Bénard convection (Fig. 12b), which is close to the convectional instability discussed here, can be also described by three differential equations (Moon, 1987).

Conclusions

Kerimasi is a rare example of carbonatites containing primary pyrochlore with exceptionally well preserved strong primary zoning. Despite an elevated U content all studied crystals are crystalline and suitable for single-crystal X-ray diffraction analysis.

Detailed study of pyrochlore from carbonatite tuff breccias and pyroclastic breccias, which are well-exposed in walls of the Loluni and Kisete craters, shows the presence of at least two compositional mineral varieties. All crystals studied are notably poor in Ta meaning that U-Ta pyrochlore, a common early crystallised mineral in calcite carbonatites from elsewhere, is absent in Kerimasi rocks. Pyrochlore from Loluni is enriched in U and light REE, particularly in Ce, at the *A* site; elevated amounts of Zr present in the *B* site and the mineral probably contains significant concentration of O, in addition to F, in the *Z* site. The mineral variety from Kisete is essentially Na-Ca pyrochlore, although it contains some U in the *A* site; the *B* site contains a significant amount of Ti and F is the dominant anion in *Z* site with a low concentration of (OH). There is also a difference in concentration of minor elements like Mg (present in Loluni pyrochlore) and Si (present in Kisete pyrochlore). These observations suggest that Loluni and Kisete carbonatites were crystallised from compositionally different carbonatitic melts. They could be independent melt batches or related one to another by fractionation; early baddeleyite crystallization could be important process controlling Zr content in a carbonatite melt. However, detailed mineralogical and geochemical studies are needed to prove a particular model. Zoning patterns and compositional data for Zr-bearing pyrochlore from Loluni indicate melt enrichment in Zr at an early stage of mineral crystallization, with baddeleyite as the first mineral to crystallize, followed by pyrochlore or kerimasite.

Prepublished Article

The characteristic feature of the Kerimasi pyrochlore is strong compositional inhomogeneity manifesting itself in oscillatory and sector zoning. While oscillatory zoning is relatively common in pyrochlore, the presence of sector zoning was previously observed in carbonatites from São Vicente Island only (Hodgson and Le Bas, 1992). The likely reason for the absence of sector zoning in other locations is the absence of coexistent well developed {111} and {100} growth sectors that are controlled by the chemical composition and growth conditions. In this respect it is worth noting that pyrochlore from Loluni and São Vicente has a nearly identical chemical composition. Formation of the sector zoning can be explained by the preferential incorporation of smaller and higher charged elements into more geometrically constrained sites on the growing surfaces (Dowty, 1976). This pattern works well for most of elements, some discrepancies are likely to be associated with complex element substitution schemes simultaneously affecting *A* and *B* sites. The oscillatory zoning in pyrochlore from Kerimasi as well as from other locations is not consistent with the majority of mechanisms proposed to explain this phenomenon, such as sudden temperature variations, pressure release, or loss of volatile components; periodic magma injections and magma mixing; or diffusion-attachment instabilities at the growth front. Instead it can be rationalised by considering convectional instabilities of carbonatite magmas during pyrochlore crystallization in dykes.

Preprinted Article

Acknowledgements. We would like to thank Structural Editor Peter Leverett, Benjamin Walter, two anonymous reviewers and Principal Editor Roger Mitchell for their critical reviews that improve the manuscript. This study was supported by the Marie Curie Fellowship (FP6) and Alexander von Humbolt Stiftung (field works), St. Petersburg State University (Pure ID 36259478) and The Natural History Museum (London). Technical support by the X-ray Diffraction and Geomodel Resource Centres (St. Petersburg State University) is gratefully acknowledged. Funding from the European Union's Horizon 2020 research and innovation programme under grant agreement No. 689909 to present this paper at the HiTech AlkCarb end of project meeting is gratefully acknowledged. The authors thank Frances Wall for the comments on the final version of the manuscript.

References

Albarede F. and Bottinga Y. (1972) Kinetic disequilibrium in trace element partitioning between phenocryst and host lava. *Geochimica et Cosmochimica Acta*, **36**, 141–156.

Atencio D., Andrade M.B., Christy A.G., Gieré R., and Kartashov P.M. (2010) The pyrochlore supergroup of minerals: nomenclature. *The Canadian Mineralogist*, **48**, 673–698.

Belyatsky B.V., Lepekhina E.N., Antonov A.V., Rodionov N.V., Nedosekova I.L., Petrov O.V.,

Shevchenko S.S. and Sergeev S.A. (2018) The age of Nb rare-metal mineralization of the Ilmeny–Vishnevogorsky alkaline complex (South Urals). *Doklady Earth Sciences*, **481** (2), 1079–1085.

Bonazzi P., Bindi L., Zoppi M., Capitani G.C. and Olmi F. (2006) Single-crystal diffraction and transmission electron microscopy studies of "silicified" pyrochlore from Narssârssuk, Julianehaab district, Greenland. *American Mineralogist*, **91**, 794–801.

Cámara F., Williams C.N., Della Ventura G., Oberti R. and Caprilli E. (2004) Non-metamict betafite from Le Carcarelle (Vico volcanic complex, Italy): occurrence and crystal structure. *Mineralogical Magazine*, **68**, 939–950.

Caprilli E., Della Ventura G., Williams T.C., Parodi G.C. and Tucceimeu P. (2006) The crystal chemistry of non-metamict pyrochlore-group minerals from Latium, Italy. *The Canadian Mineralogist*, **44**, 1367–1378.

Černý P., Hawthorne F.C., Laflamme J.H.G. and Hinthorne J.R. (1979) Stibiobetafite, a new member of the pyrochlore group from Vezná, Czechoslovakia. *The Canadian Mineralogist*, **17**, 583–588.

Chakhmouradian A.R. and Zaitsev A.N. (1999) Calcite-amphibole-clinopyroxene rock from the Afrikanda Complex, Kola Peninsula, Russia: mineralogy and a possible link to carbonatites: I, oxide minerals. *The Canadian Mineralogist*, **37**, 177–198.

Chakhmouradian A.R. and Mitchell R.H. (2002) New data on pyrochlore- and perovskite-group minerals from the Lovozero alkaline complex, Russia. *European Journal of Mineralogy*, **14**, 821–836.

Chakhmouradian A.R. and Williams C.T. (2004) Mineralogy of high-field-strength elements (Ti, Nb, Zr, Ta, Hf) in phoscoritic and carbonatitic rocks of the Kola Peninsula, Russia. Pp. 293–340 in: *Phoscorites and Carbonatites From Mantle to Mine: The Key Example of th*e Kola Alkaline Province (F. Wall and A.N. Zaitsev, editors). The Mineralogical Society Series 10.

Chakhmouradian A.R., Halden N.M., Mitchell R.H. and Horváth L. (2007) Rb-Cs-rich rasvumite and sector-zoned "loparite-(Ce)" from Mont Saint-Hilaire (Québec, Canada) and their petrologic significance. *European Journal of Mineralogy*, **19**, 533–546.

Chakhmouradian A.R., Reguir E.P., Kressall, R.D., Crozier J., Pisiak L.K., Sidhu R. and Yang P. (2015) Carbonatite-hosted niobium deposit at Aley, northern British Columbia (Canada): mineralogy, geochemistry and petrogenesis. *Ore Geology Reviews*, **64**, 642–666.

Chakhmoradian A.R., Reguir E.P. and Zaitsev A.N. (2016) Calcite and dolomite in intrusive carbonatites. I. Textural variations. *Mineralogy and Petrology*, **110**, 333–360.

Chakhmouradian A.R., Reguir E.P., Zaitsev A.N., Couëslan C., Xue C., Kynický J., Mumin

Prepublished Article

A.H. and Yang P. (2017) Apatite in carbonatitic rocks: compositional variation, zoning, element partitioning and petrogenetic significance. *Lithos*, **274–275**, 188–213.

Chernov, A.A. (1984) *Modern Crystallography III. Crystal growth*. Springer, Berlin.

Christy A.G. and Atencio D. (2013) Clarification of status of species in the pyrochlore supergroup. *Mineralogical Magazine*, **77**, 13–20.

Church A.A. (1995) *The petrology of the Kerimasi Carbonatite Volcano and the carbonatites of Oldoinyo Lengai with a review of other occurrences of extrusive carbonatites*. PhD dissertation, University of London, London, UK.

Cressey G., Wall F. and Cressey B.A. (1999) Differential REE uptake by sector growth of monazite. *Mineralogical Magazine*, **63**, 813–828.

Dawson J.B. (2008) *The Gregory Rift Valley and Neogene-Revent Volcanoes of Northern Tanzania*. Geological Society, London Geological Society Memoir No. 33, 102 p.

Dawson J.B. and Powell D.G. (1969) The Natron-Engaruka explosion crater area, Northern Tanzania. *Bulletin Volcanologique*, **33**, 791–817.

Dawson J.B., Steele I.M., Smith J.V. and Rivers M.L. (1996) Minor and trace element chemistry of carbonates, apatites and magnetites in some African carbonatites. *Mineralogical Magazine*, **60**, 415–425.

Deans T. and Roberts B. (1984) Carbonatite tuffs and lava clasts of the Tinderet foothills, western Kenya: a study of calcified natrocarbonatites. *Journal of the Geological Society, London*, **141**, 563–580.

Delcamp A., Delvaux D., Kwelwa S., Macheyeki A. and Kervyn M. (2016) Sector collapse events at volcanoes in the North Tanzanian divergence zone and their implications for regional tectonics. *Geological Society of America Bulletin*, **128**, 169–186.

Dolomanov O.V., Bourhis L.J., Gildea R.J., Howard J.A.K. and Puschmann H. (2009) *OLEX2*: a complete structure solution, refinement and analysis program. *Journal of Applied Crystallography*, **42**, 339–341.

Dowty E. (1976) Crystal structure and crystal growth II. Sector zoning in minerals. *American Mineralogist*, **61**, 460–469.

Grassberger P. and Procaccia I. (1984) Dimensions and entropies of strange attractors from a fluctuating dynamics approach. *Physica D*, **13**, 34–54.

Guteneva V.S. (2012) *Crystal chemistry of complex oxides from the Khibina alkaline massif*. Master thesis, St. Petersburg State University, St. Petersburg, Russia. (in Russian).

Guzmics T., Mitchell R.H., Szabó C., Berkesi M., Milke R. and Abart R. (2011) Carbonatite melt inclusions in coexisting magnetite, apatite and monticellite in Kerimasi calciocarbonatite, Tanzania: melt evolution and petrogenesis. *Contribution to Mineralogy*

Prepublished Article

and Petrology, **161**, 177–196.

Guzmics T., Mitchell R.H., Szabó C., Berkesi M., Milke R. and Ratter K. (2012) Liquid immiscibility between silicate, carbonate and sulfide melts in melt inclusions hosted in co-precipitated minerals from Kerimasi volcano (Tanzania): evolution of carbonated nephelinitic magma. *Contributions to Mineralogy and Petrology*, **164**, 101–122.

Hay R.L. (1983) Natrocarbonatite tephra of Kerimasi volcano, Tanzania. *Geology*, **11**, 599–602.

Hodgson N.A. and Le Bas M. J. (1992) The geochemistry and cryptic zonation of pyrochlore from San Vicente, Cape Verde Islands. *Mineralogical Magazine*, **56**, 201–214.

Hogarth D.D. (1977) Classification and nomenclature of the pyrochlore group minerals. *American Mineralogist*, **62**, 403–410.

Hogarth D.D. (1989) Pyrochlore, apatite and amphibole: distinctive minerals in carbonatites. Pp. 105–148 in: *Carbonatites: Genesis and Evolution* (K. Bell, editor). Chapman and Hall, London.

Hogarth D.D. and Horne J.E.T. (1989) Non-metamict uranoan pyrochlore and uranpyrochlore from tuff near Ndale, Fort Portal area, Uganda. *Mineralogical Magazine*, **53**, 257–262.

Hogarth D.D., Williams C.T. and Jones P. (2000) Primary zoning in pyrochlore group minerals from carbonatites. *Mineralogical Magazine*, **64**, 683–697.

Hollister L.S. (1970) Origin, mechanism, and consequences of compositional sector zoning in staurolite. *American Mineralogist*, **55**, 742–766.

Hollister L.S. and Gancarz A. (1971) Compositional sector-zoning in clinopyroxene from the Narce Area, Italy. *American Mineralogist*, **56**, 959–979.

Ivanyuk G.Y., Konoplyova N.G, Yakovenchuk V.N., Pakhomovsky Y.A., Panikorovskii T.L., Kalashnikov A.O., Bocharov V.N., Bazai A.V., Mikhailova J.A. and Goryainov P.M. (2018) Three-D mineralogical mapping of the Kovdor phoscorite-carbonatite complex, NW Russia: III. Pyrochlore Supergroup Minerals. *Minerals*, **8**, 277.

Ivanyuk G.Y., Yakovenchuk V.N., Panikorovskii T.L., Konoplyova N., Pakhomovsky Y.A., Bazai A.V., Bocharov V.N. and Krivovichev S.V. (2019) Hydroxynatropyrochlore, $(Na,Ca,Ce)_2Nb_2O_6(OH)$, a new member of the pyrochlore group from the Kovdor phoscorite-carbonatite pipe, Kola Peninsula, Russia. *Mineralogical Magazine*, **83**, 107–113.

Kalischewski F., Lubashevsky I. and Heuer A. (2007) Boundary-reaction-diffusion model for zoning in binary crystals grown from solution. *Physical Reviews E*, **75**, 021601.

Kapustin Yu.L. (1980) *Mineralogy of Carbonatites*. Amerind Publishing, New Delhi, 259 pp.

Kasatkin A.V., Britvin S.N., Peretyazhko I.S. and Chukanov N.V. (2020) Oxybismutomicrolite, a new pyrochlore-supergroup mineral from the Malkhan pegmatite field, Central

Preprinted Article

Transbaikalia, Russia. *Mineralogical Magazine*, **84**, 444–454.

Kervyn M., Ernst G.G.J., Klaudius J., Keller J., Mbede E. and Jacobs P. (2008) Remote sensing study of sector collapses and debris avalanche deposits at Oldoinyo Lengai and Kerimasi volcanoes, Tanzania. *International Journal of Remote Sensing*, **29** (22), 6565–6595.

Lee M.J., Lee J.L., Garcia D., Moutte J., Williams C.T. Wall F. and Kim Y. (2006) Pyrochlore chemistry from the Sokli phoscorite–carbonatite complex, Finland: implications for the genesis of phoscorite and carbonatite association. *Geochemical Journal*, **40**, 1–13.

L'Heureux I. and Fowler A.D. (1994) A nonlinear model of oscillatory zoning in plagioclase. American Mineralogist, 79, 885–891.

L'Heureux I. and Katsev S. (2006) Oscillatory zoning in a $(Ba,Sr)SO_4$ solid solution: Macroscopic and cellular automata models. *Chemical Geology*, **225**, 230–243.

Li G., Yang G., Lu F., Xiong M., Ge X., Pan B. and Fourestier J.D. (2016) Fluorcalciopyrochlore, a new mineral species from Bayan Obo, Inner Mongolia, P.R. China. *The Canadian Mineralogist*, **54**, 1285–1291.

Macintyre R.M., Mitchell J.G and Dawson J.B. (1974) Age of fault movements in Tanzanian sector of East African Rift system. Nature, 247, 354–356.

Mariano A.N. and Roeder P.L. (1983) Kerimasi: a neglected carbonatite volcano. *Journal of Geology*, **91**, 449–455.

Melgarejo J.C., Costanzo A., Bambi A.C.J.M., Gonçalves A.O. and Neto A.B. (2012) Subsolidus processes as a key factor on the distribution of Nb species in plutonic carbonatites: the Tchivira case, Angola. *Lithos*, **152**, 187–201.

Mitchell R.H. (2015) Primary and secondary niobium mineral deposits associated with carbonatites. *Ore Geology Reviews*, **64**, 626–641.

Mitchell R.H., Wahl R., and Cohen A. (2020) Mineralogy and genesis of pyrochlore apatitite from The Good Hope Carbonatite, Ontario: A potential niobium deposit. *Mineralogical Magazine*, **84**, 81–91.

Moon F.C. (1987) *Chaotic vibrations*. Wiley, NY.

Nasraoui M. and Bilal E. (2000) Pyrochlores from the Lueshe carbonatite complex (Democratic Republic of Congo): a geochemical record of different alteration stages. *Journal of Asian Earth Sciences*, **18**, 237–251.

Paquette J. and Reeder R.J. (1990) New type of compositional zoning in calcite: insights into crystal-growth mechanisms. *Geology*, **18**, 1244–1247.

Perugini D., Poli G. and Mazzuoli R. (2003) Chaotic advection, fractals and diffusion during mixing of magmas: evidence from lava flows. *Journal of Volcanology and Geothermal Research*, **124**, 255–279.

Prepublished Article

Perugini D., Poli G. and Valentini L. (2005) Strange attractors in plagioclase oscillatory zoning: Petrological implications. *Contributions to Mineralogy and Petrology*, **149**, 482–497.

Popov V.N., Tsivinskaya Yu.S., Bekker T.B., Kokh K.A. and Kokh A.E. (2006) Numerical investigation of heat-mass transfer processes in hydrothermal growth system. *Journal of Crystal Growth*, **289**, 652–658.

Rakovan J. and Reeder R.J. (1994) Differential incorporation of trace elements and dissymmetrization in apatite: the role of surface structure during growth. *American Mineralogist*, **79**, 892–903.

Reguir E.P., Chakhmouradian A.R., Nalden N.M., Yang P. and Zaitsev A.N. (2008) Early magmatic and reaction-induced trends in magnetite from the carbonatites of Kerimasi, Tanzania. *The Canadian Mineralogist*, **46**, 879–900.

Rouse R.C., Dunn P.J., Peacor D.R. and Wang L. (1998) Structural studies of the natural antimonian pyrochlores. I. Mixed valency, cation site splitting, and symmetry reduction in lewisite. *Journal of Solid State Chemistry*, **141**, 562–569.

Shannon R.D. (1976) Revised effective ionic radii and systematic studies of interatomic distances in halides and chalcogenides. *Acta Crystallographica*, **A32**, 751–767.

Sharygin V.V., Sobolev N.V. and Channer D.M.DeR. (2009) Oscillatory-zoned crystals of pyrochlore-group minerals from the Guaniamo kimberlites, Venezuela. *Lithos*, **112S**, 976–985.

Sheldrick G.M. (2015) Crystal structure refinement with *SHELXL*. *Acta Crystallographica*, **C71**, 3–8.

Shore M. and Fowler A.D. (1996) Oscillatory zoning in minerals: a common phenomenon. *The Canadian Mineralogist*, **34**, 1111–1126.

Shtukenberg A.G. and Punin Yu.O. (2011) Micromorphological instability of a growing face as a source of oscillatory zoning in crystals. *Mineralogical Magazine*, **75**, 169–183.

Shtukenberg A.G., Popov D.Yu. and Punin Yu.O. (2005) Growth ordering and anomalous birefringence in ugrandite garnets. *Mineralogical Magazine*, **69**, 537–550.

Shtukenberg A.G., Punin Yu.O. and Artamonova O.I. (2009) Effect of crystal composition and growth rate on sector zoning in solid solutions grown from aqueous solutions. *Mineralogical Magazine*, **73**, 385–398.

Subbotin V.V. and Subbotina G.F. (2000) Minerals of the pyrochlore group in phoscorites and carbonatites of the Kola Peninsula. [*Proceedings of the Murmansk State Technical University*], **3** (2), 273–284.

Tappe S., Steenfelt A., Heaman L.M. and Simonetti A. (2009) The newly discovered Jurassic Tikiusaaq carbonatite-aillikite occurrence, West Greenland, and some remarks on

Prepublished Article

carbonatite–kimberlite relationships. *Lithos*, **112S**, 385–399.

Tauson V.L. (2005) On the formation of growth sector zoning in izomorphous mixed crystals. *Geochemistry International*, **43**, 410-413.

Tiller W.A. (1986) The role of strongly interface/surface adsorbed impurities on the purification process via crystallization methods. *Journal of Crystal Growth*, **75**, 132–138.

Tiller W.A. and Ahn K.-S. (1980) Interface field effects on solute redistribution during crystallization. *Journal of Crystal Growth*, **49**, 483–501.

Treiman A.H. (1989) Carbonatite magma: properties and processes. In Bell K. (ed.) *Carbonatites. Genesis and Evolution*. Unwin Hyman Ltd. p. 89–104.

Viladkar S.G., Bismayer U. and Ziietlow P. (2017) Metamict U-rich pyrochlore of Newania carbonatite, Udaipur, Rajasthan. *Journal Geological Society of India*, **89**, 133–138.

Voloshin A.V, Pakhomovskiy Ya.A., Pushcharovskiy D.Yu., Nadezhina T.N., Bakhchisaraitsev A.Yu. and Kobyashev Yu.S. (1989) Strontiopyrochlore: composition and structure. *New Data on Minerals*, **36**, 12–24. (in Russian).

Wall F., Williams C.T., Woolley A.R. and Nasraoui M. (1996) Pyrochlore from weathered carbonatite at Lueshe, Zaire. *Mineralogical Magazine*, **60**, 731–750.

Walter B.F., Parsapoor A., Braunger S., Marks M.A.W., Wenzel T., Martin M and Markl G. (2018) Pyrochlore as a monitor for magmatic and hydrothermal processes in carbonatites from the Kaiserstuhl volcanic complex (SW Germany). *Chemical Geology*, **498**, 1–16.

Wetzel F., Schmitt A.K., Kronz A. and Wörner G. (2010) In situ ^{238}U-^{230}Th disequilibrium dating of pyrochlore at sub-millennial precision. *American Mineralogist*, **95**, 1353–1356.

Wiedenmann D., Zaitsev A.N., Britvin S.N., Krivovichev S.V. and Keller J. (2009) Alumoåkermanite, $(Ca,Na)_2(Al,Mg,Fe^{2+})(Si_2O_7)$, a new mineral from the active carbonatite–nephelinite–phonolite volcano Oldoinyo Lengai, northern Tanzania. *Mineralogical Magazine*, **73**, 373–384.

Wiedenmann D., Keller J. and Zaitsev A.N. (2010) Melilite-group minerals at Oldoinyo Lengai, Tanzania. *Lithos*, **118**, 112–118.

Yaroshevskii A.A. and Bagdasarov Yu.A. (2008) Geochemical diversity of minerals of the pyrochlore group. *Geochemistry International*, **46**, 1245–1266.

Zaitsev A.N. (2010) Nyerereite from calcite carbonatite of Kerimasi volcano, northern Tanzania. *Geology of Ore Deposits*, **52** (7), 630–640.

Zaitsev A.N., Keller J., Spratt J., Perova E.N. and Kearsley A. (2008) Nyerereite-pirssonite-calcite-shortite relationships in altered natrocarbonatites, Oldoinyo Lengai, Tanzania. *The Canadian Mineralogist*, **46**, 843–860.

Zaitsev A.N., Williams C.T., Britvin S.N., Kuznetsova I.V., Spratt J., Petrov S.V. and Keller J.

Prepublished Article

(2010) Kerimasite, $Ca_3Zr_2(Fe^{3+}{}_2Si)O_{12}$, a new garnet from carbonatites of Kerimasi volcano and surrounding explosion craters, northern Tanzania. *Mineralogical Magazine*, **74**, 841–858.

Zaitsev A.N., Chakhmouradian A.R., Siidra O.I., Spratt J., Williams C.T., Stanley C.J., Petrov S.V., Britvin S.N. and Polyakova E.A. (2011) Fluorine-, yttrium- and lanthanide-rich cerianite-(Ce) from carbonatitic rocks of the Kerimasi volcano and surrounding explosion craters, Gregory Rift, northern Tanzania. *Mineralogical Magazine*, **75**, 2813–2822.

Zaitsev A.N., Williams C.T., Wall F. and Zolotarev A.A. (2012) Evolution of chemical composition of pyrochlore group minerals from phoscorites and carbonatites of the Khibina alkaline massif. *Geology of Ore Deposits*, **54**, 503–515.

Zaitsev A.N., Wenzel T., Vennemann T. and Markl G. (2013) Tinderet volcano, Kenya – an old natrocarbonatite locality? *Mineralogical Magazine*, **77**, 213–226.

Zaitsev A.N., Williams C.T., Jeffries T.E., Strekopytov S., Moutte J., Ivashchenkova O.V., Spratt J., Petrov S.V.,Wall F., Seltmann R. and Borozdin A.P. (2014) Rare earth elements in phoscorites and carbonatites of the Devonian Kola Alkaline Province, Russia: examples from Kovdor, Khibina, Vuoriyarvi and Turiy Mys complexes. *Ore Geology Reviews*, **61**, 204–225.

Zaitsev A.N., Spratt J., Sharygin V.V., Wenzel T., Zaitseva O.A. and Markl G. (2015) Mineralogy of the Laetolil footprint tuff: a comparison with possible volcanic sources from the Crater Highlands and Gregory rift. *Journal of African Earth Sciences*, **111**, 214–221.

Zurevinski S.E. and Mitchell R.H. (2004) Extreme composition variation in pyrochlore group minerals at the Oka Carbonatite Complex, Québec: evidence of magma mixing? *The Canadian Mineralogist*, **42**, 1159–1168.

Prepublished Article

Figure captions

Fig. 1. View of the Kerimasi volcano and the Loluni and Loolmurwak craters. Loolmurwak consists of three units: crystal-rich tuff (I), carbonatite tuff/pyroclastic breccia (II) and nephelinite tuff breccia (III). At the Loluni crater only crystal-rich tuff and carbonatite tuff/pyroclastic breccia are exposed.

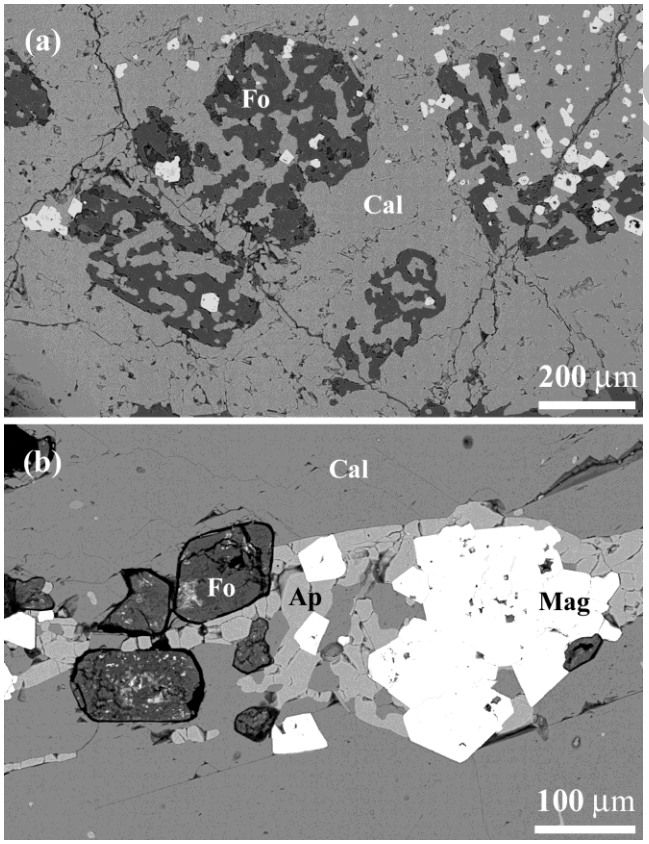

Fig. 2. Back-scattered electron images of intrusive calcite carbonatites consisting of calcite (Cal), apatite (Ap), magnetite (Mag) with (a) forsterite oikocrysts (Fo) and (b) euhedral forsterite (Fo) now fully replaced by hydrous Fe-Mg silicate.

ed Article

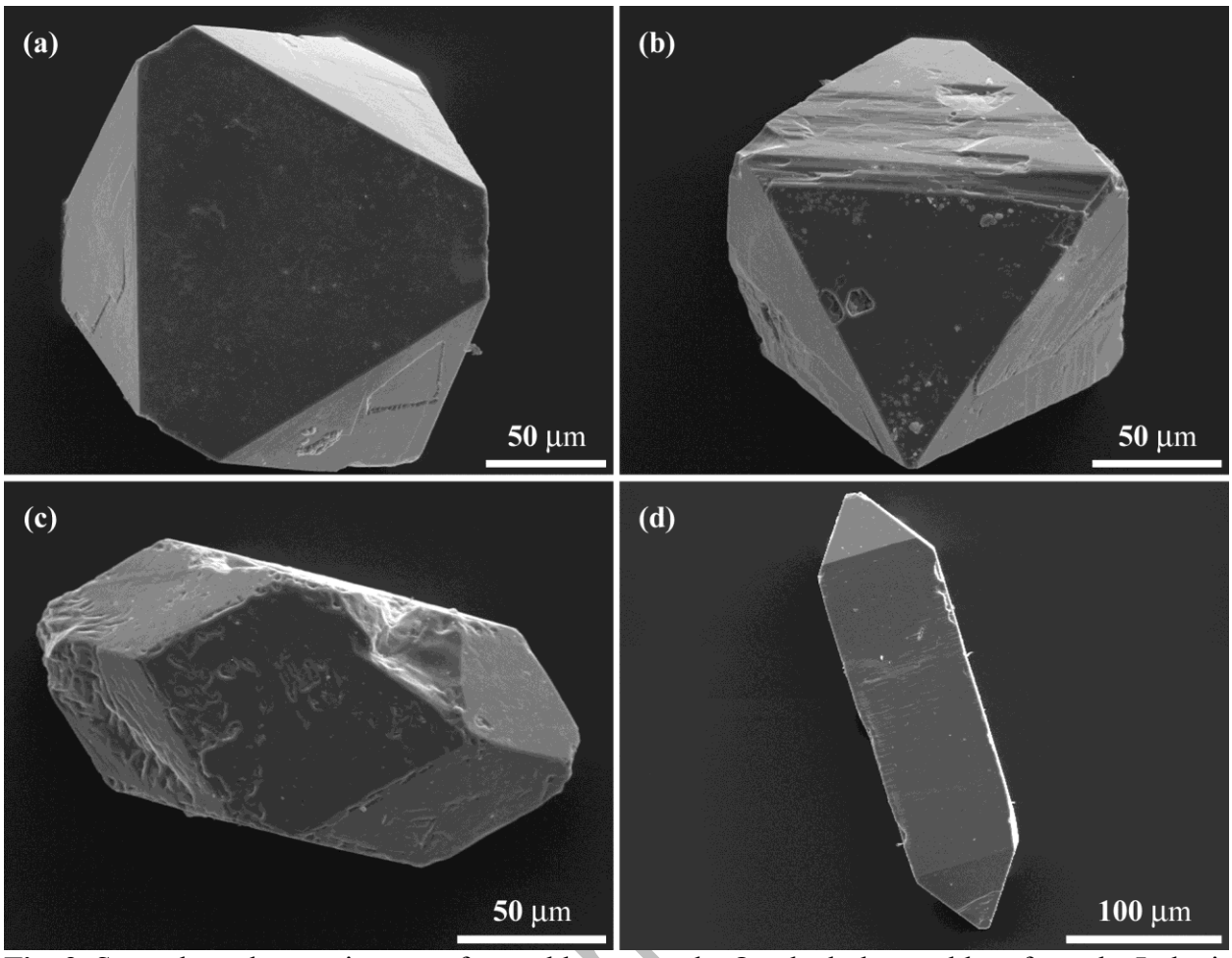

Fig. 3. Secondary electron images of pyrochlore crystals. Octahedral pyrochlore from the Loluni (a) and Kisete (b) craters, cubo-octahedral pyrochlore (c, d) from the Kisete crater.

Prepublish

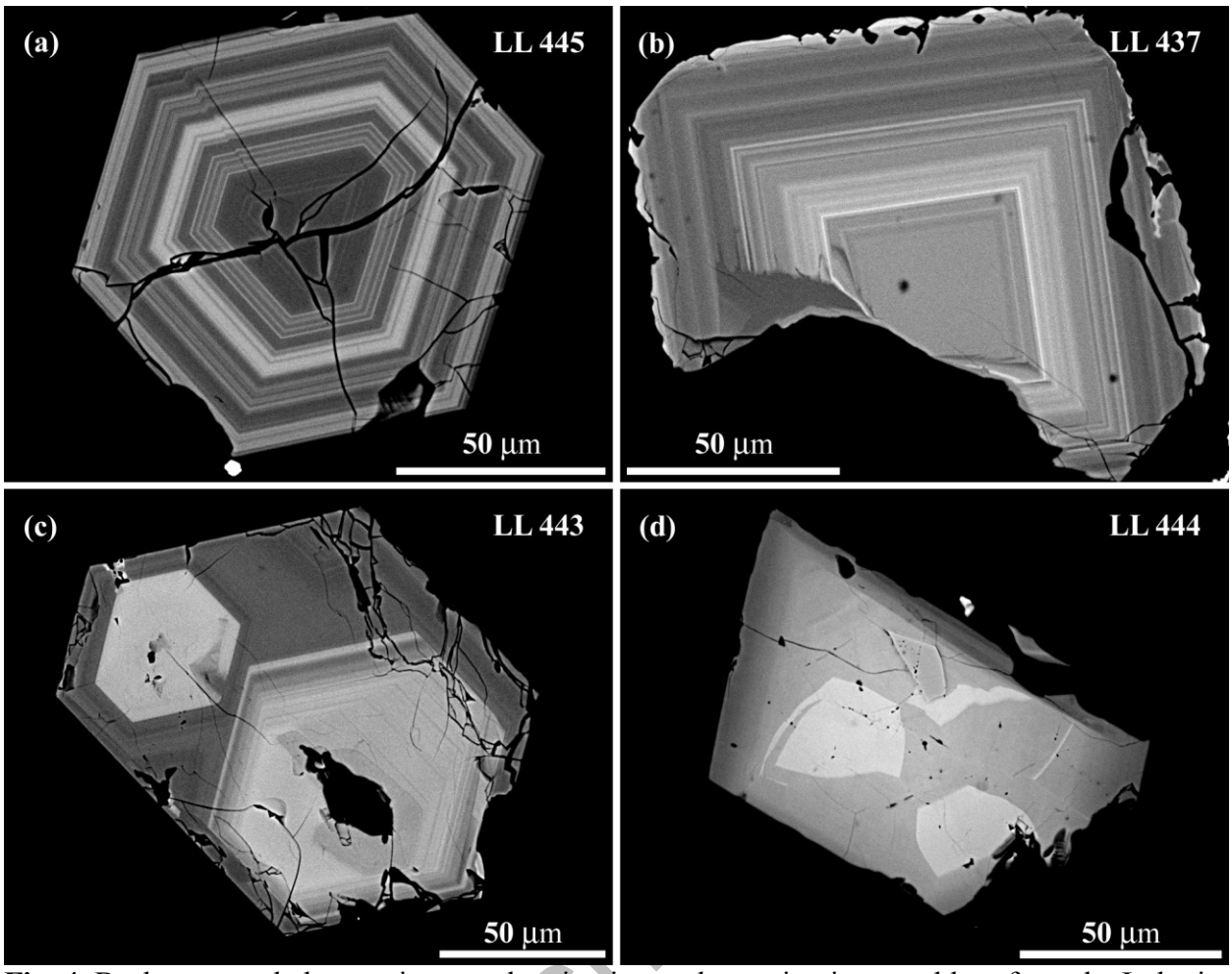

Fig. 4. Back-scattered electron images showing internal zonation in pyrochlore from the Loluni crater.

Prepublish

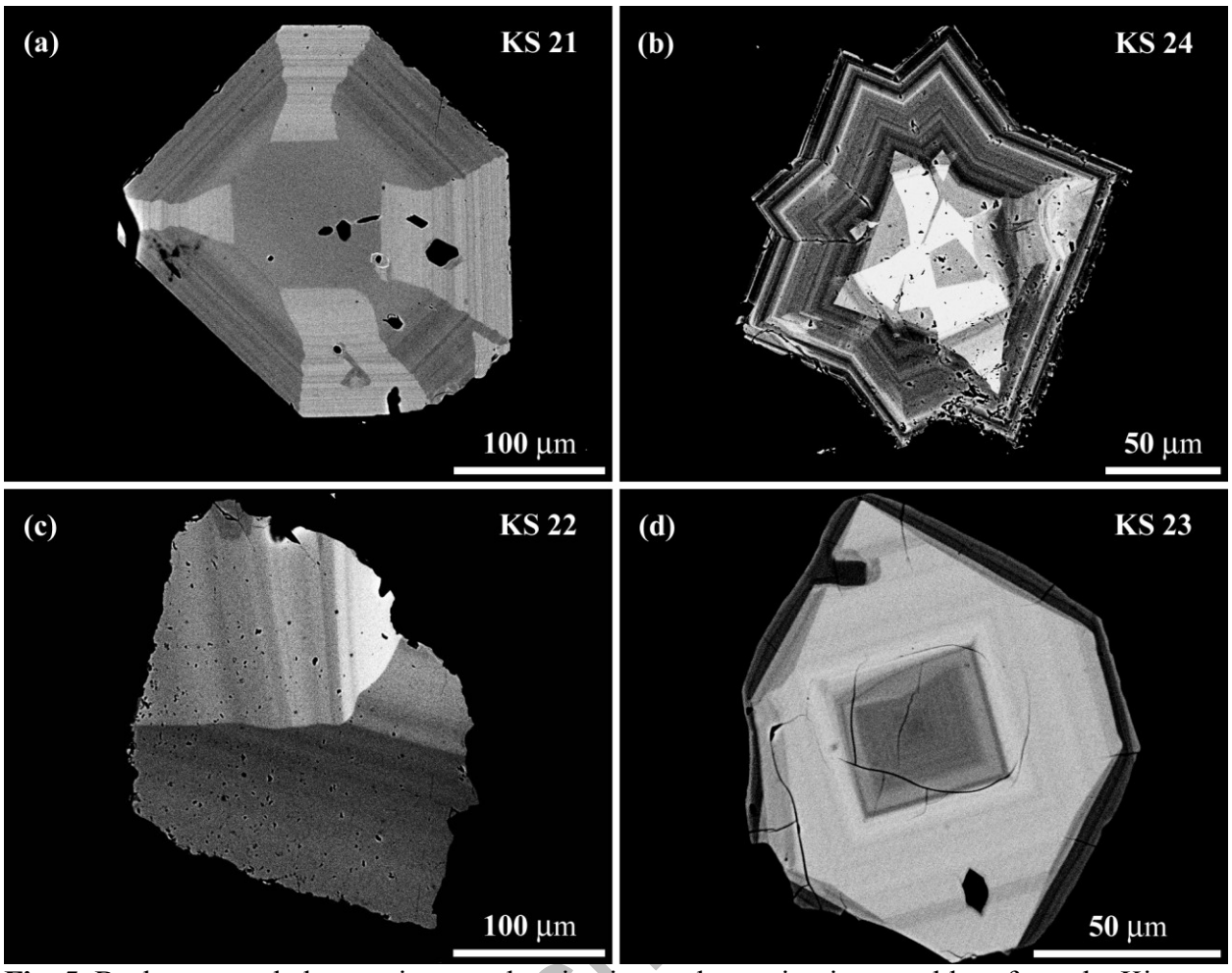

Fig. 5. Back-scattered electron images showing internal zonation in pyrochlore from the Kisete crater.

Prepublish

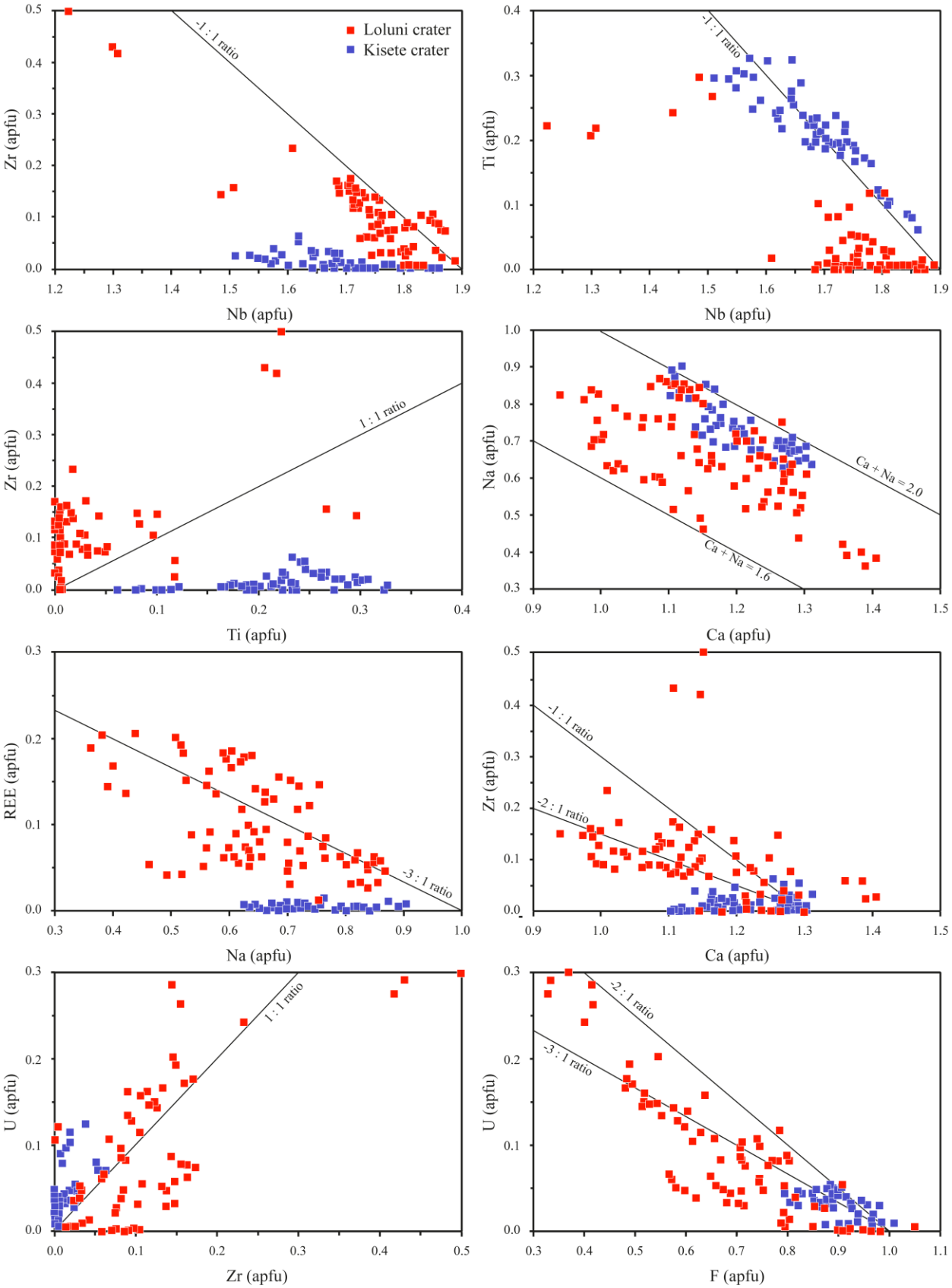

Fig. 6. Compositional variations of pyrochlore from the Loluni and Kisete craters.

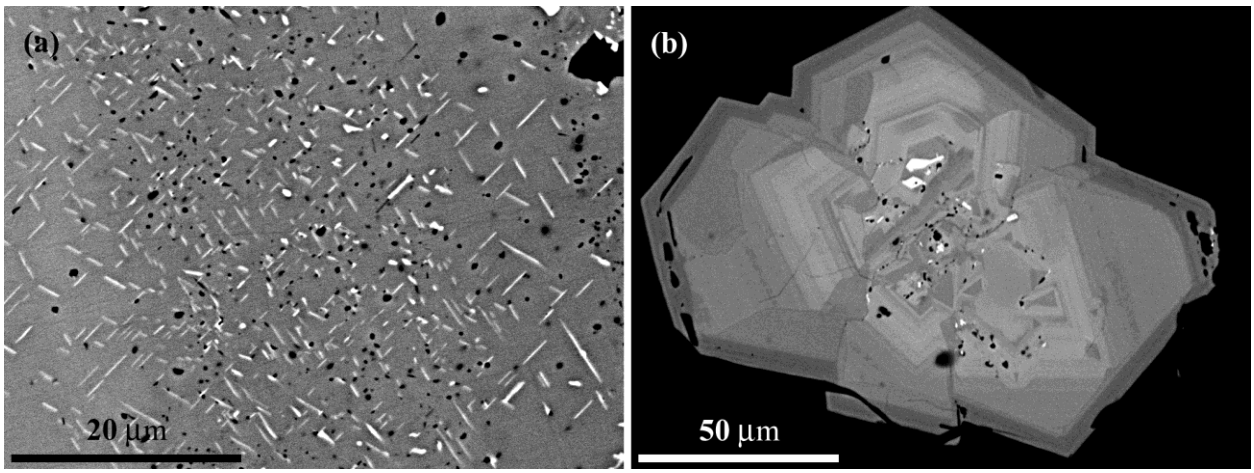

Fig. 7. Back-scattered electron images showing (a) exsolved baddeleyite (white) in pyrochlore from the Kovdor calcite carbonatite; (b) relict baddeleyite (white) in pyrochlore from the Loluni crater.

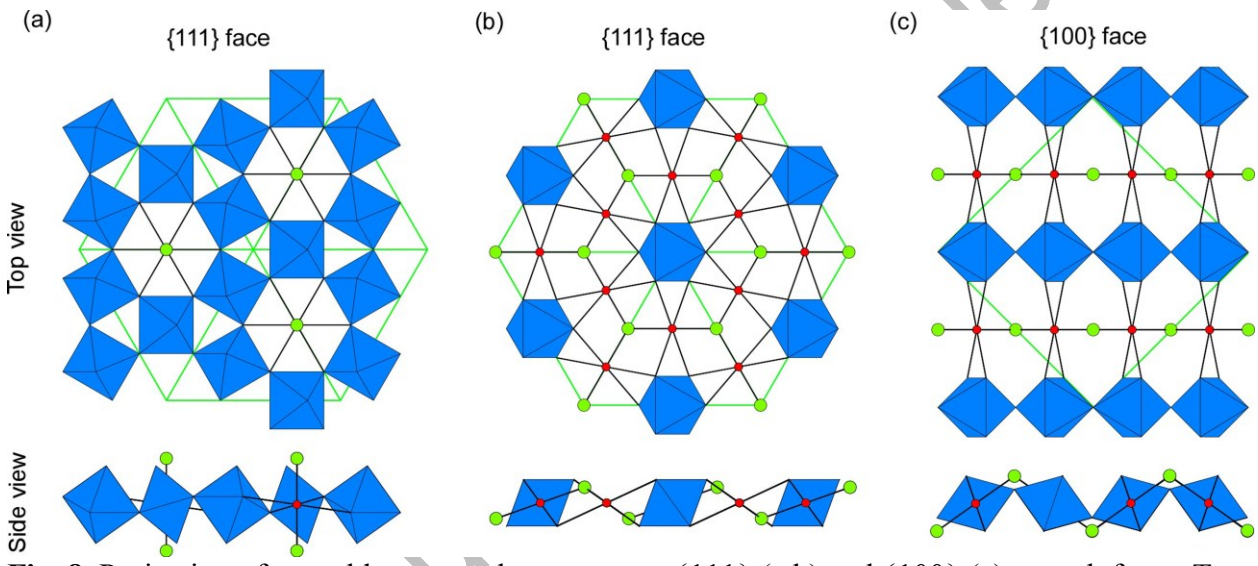

Fig. 8. Projection of pyrochlore crystal structure on {111} (a,b) and {100} (c) growth faces. Two types of blue octahedra – groups BO_6, small red balls – A sites, large green balls – (OH,F) sites. The edges of unit cell are depicted in green.

Prepu

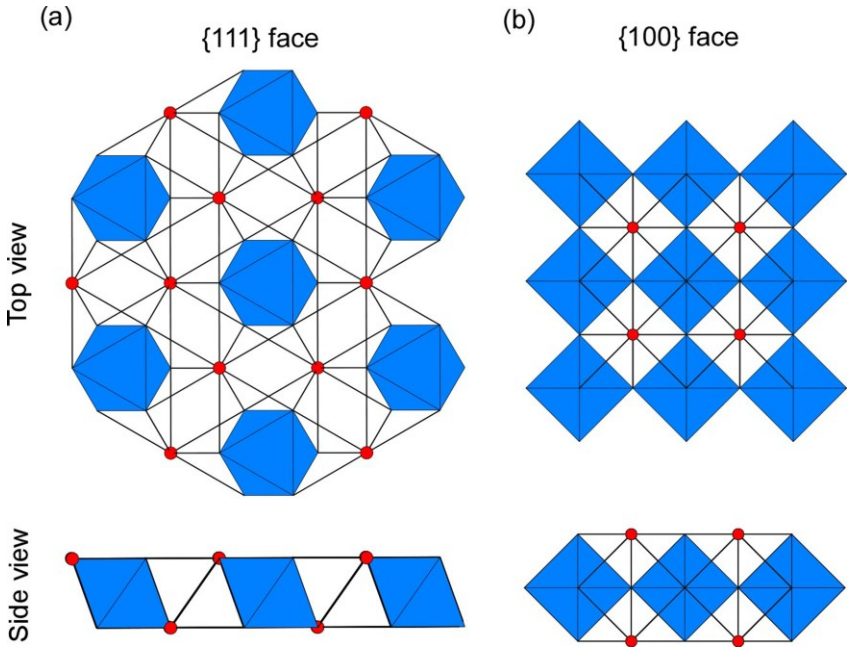

Fig. 9. Projection of perovskite crystal structure on {111} (a) and {100} (b) growth faces. Blue octahedra – groups BO_6, red balls – A sites.

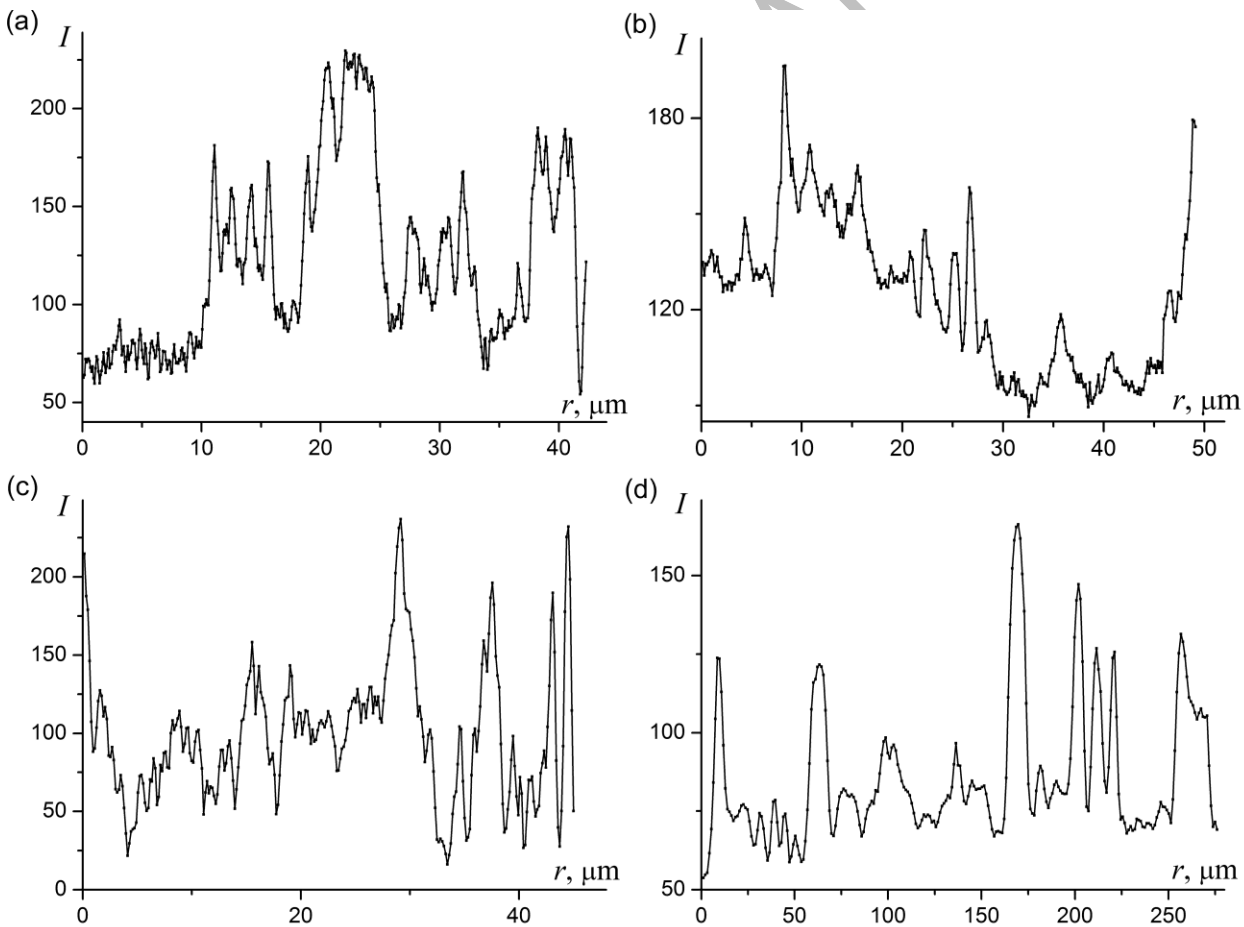

Fig. 10. Brightness of BSE image (*I*, gray scale levels) *vs*. the distance from the crystal core *r*. (a) sample LL 445, see Fig. 4a; (b) sample LL 437, see Fig. 4b; (c) sample KS 24, see Fig. 5b; (d) crystal from Fig. 2c from Hogarth *et al*. (2000).

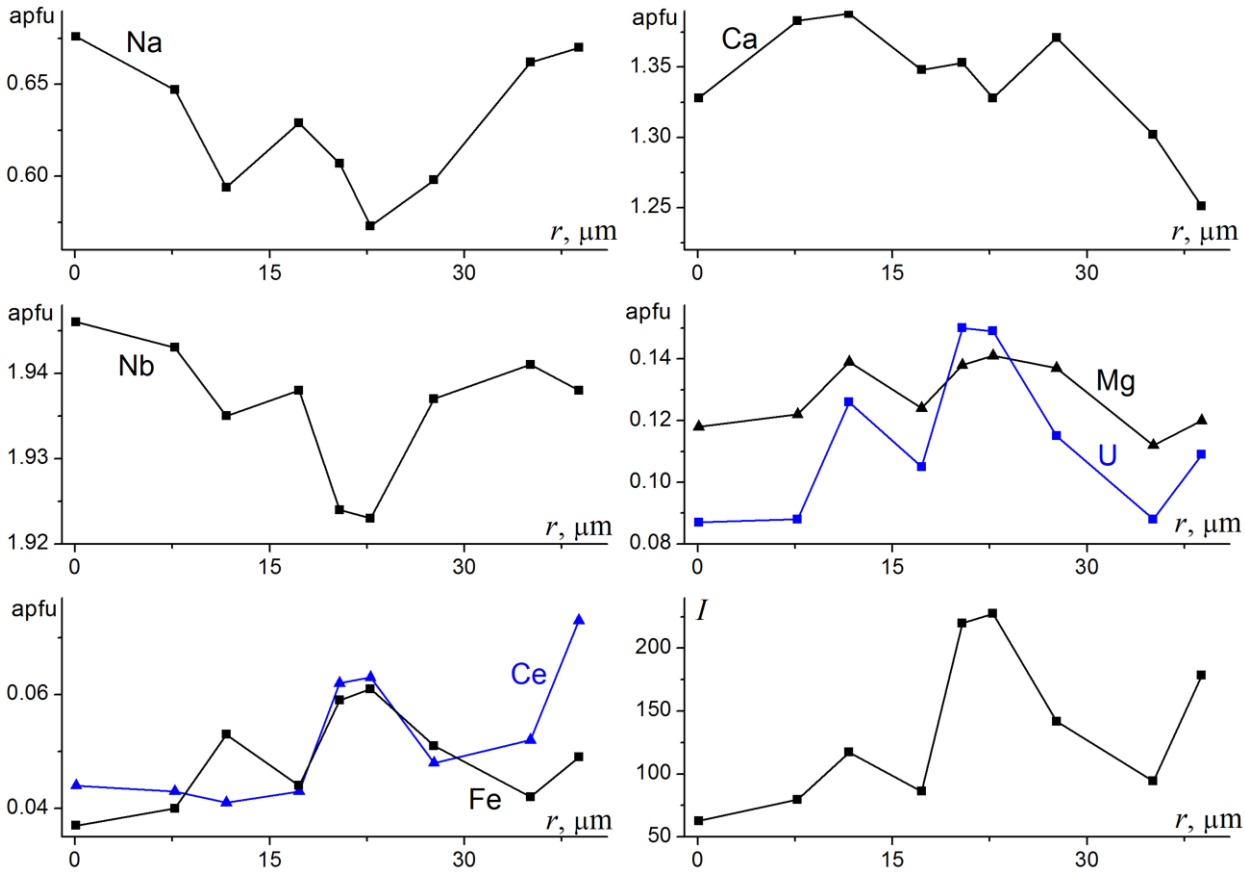

Fig. 11. Pyrochlore composition (Na, Nb, Ce, Fe, Ca, Mg and U, apfu) and brightness of BSE image (*I*, gray scale levels) plotted as a distance from the crystal center (*r*, μm) for the sample LL 445. Location of points is shown in Supplementary Figure 1b, the whole BSE profile is shown in Fig. 10a.

Prepublished

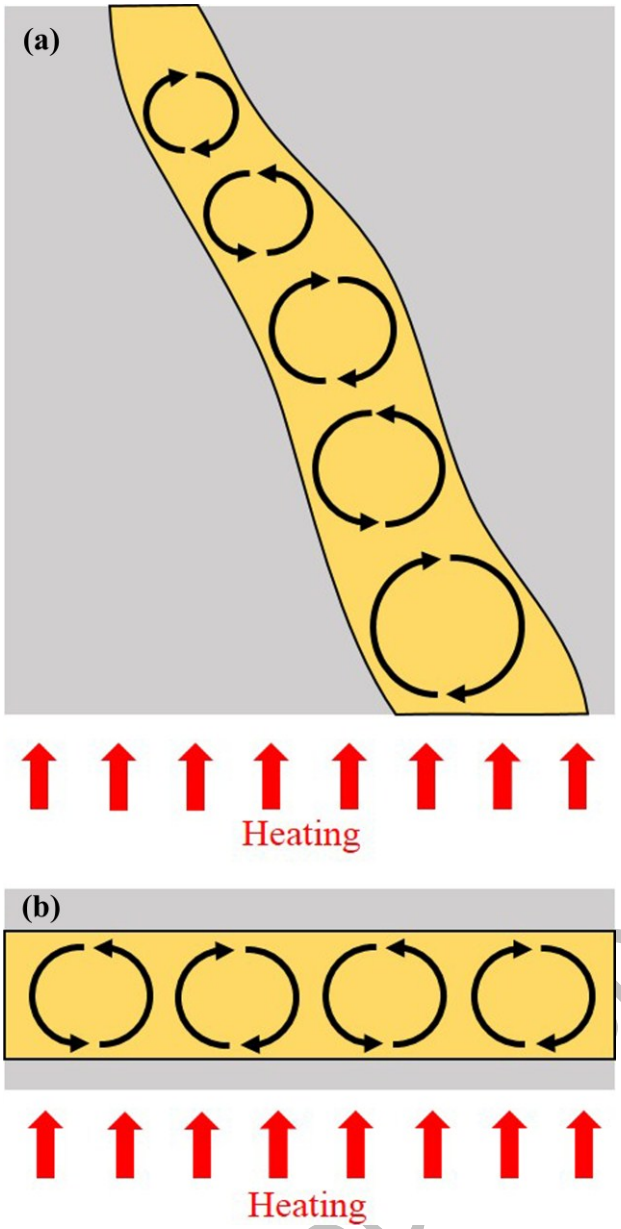

Fig. 12. Schematic illustration of convectional currents forming (a) in a dyke (sub-vertical flat layer heated from below) and (b) in a horizontal flat layer heater from below.

Pre-Published Article

Table 1. Representative compositions of pyrochlore.

Crystal	LL 445					LL 442			LL 433		LL 443		
Image	Fig. 4a										Fig. 4d		
Morphology	octahedral					octahedral			octahedral		octahedral		
Zonation	oscillatory-type					oscillatory-type			oscillatory-type		oscillatory-type		
Position	core		→		rim	core	core	rim	core	rim	core	core	rim
Point	24	26	29	31	32	1	3	10	82	81	11	13	16
wt.%													
Na_2O	5.12	4.34	4.15	5.04	4.97	6.89	7.13	7.02	5.22	5.35	4.17	5.02	5.87
K_2O											0.05		
CaO	18.20	18.34	17.41	17.93	16.78	16.89	16.93	16.48	15.91	16.37	18.11	18.84	18.39
MnO	0.16	0.21	0.25	0.08	0.16					0.08	0.26	0.23	0.13
SrO	0.44	0.09	0.11	0.41	0.34	0.46	0.72	0.46	0.29	0.10	0.36	0.21	0.31
BaO											0.08		0.07
Y_2O_3	0.12		0.20	0.18	0.16				0.13	0.24	0.27		
La_2O_3	0.36	0.35	0.50	0.48	0.61	0.48	0.29	0.42	0.76	0.63	0.69	0.51	0.27
Ce_2O_3	1.77	1.58	2.41	2.09	2.86	1.82	1.04	1.71	4.00	3.74	4.48	2.99	1.79
Pr_2O_3	0.10				0.15				0.18	0.18	0.19		
Nd_2O_3	0.21	0.21	0.42	0.26	0.31	0.35	0.11	0.32	0.52	0.47	0.67	0.31	0.28
Sm_2O_3				0.09					0.08	0.09		0.09	0.09
PbO	0.10							0.07			0.17		
ThO_2	0.09	0.09				0.38	0.06	0.34	0.31	0.31	0.65	0.21	0.06
UO_2	5.76	8.02	9.39	5.83	7.07	0.25	0.09	0.11	4.28	3.96	2.30	1.02	0.47
Nb_2O_5	63.22	60.62	59.74	63.36	61.63	64.27	66.73	66.03	57.62	58.31	58.76	63.90	67.71
Ta_2O_5										0.16			
TiO_2	0.10	0.06	0.15	0.14	0.12	0.09	0.32	0.10	0.23	0.33	0.09	0.09	0.12
ZrO_2	0.03		0.12		0.06	3.17	2.28	2.37	5.13	4.65	4.63	1.37	0.47
HfO_2													

Prepublished Article

This is a 'preproof' accepted article for Mineralogical Magazine. This version may be subject to change during the production process.
DOI: 10.1180/mgm.2020.101

Fe_2O_3	0.71	1.00	1.14	0.82	0.93	0.74	0.57	0.75	1.28	1.14	1.23	1.36	0.94
MgO	1.17	1.32	1.33	1.11	1.16	0.14	0.11	0.15	0.49	0.52	0.52	0.60	0.44
Al_2O_3	0.09	0.06	0.07	0.09	0.06	0.05	0.03	0.03	0.06	0.04	0.07	0.10	0.07
SiO_2	0.07	0.04	0.03	0.04	0.03	0.11	0.16	0.10	0.03	0.07	0.08	0.09	0.04
WO_3		0.15			0.12							0.20	
F	3.84	3.76	2.88	3.50	3.43	4.62	4.70	4.79	3.60	3.61	3.43	4.04	4.61
$-O=F_2$	1.62	1.58	1.21	1.47	1.44	1.94	1.98	2.02	1.51	1.52	1.44	1.70	1.94
Total	100.01	98.67	98.97	99.97	99.46	98.75	99.30	99.24	98.60	98.83	99.74	99.47	100.13
Structural formulae calculated on the basis of 2 *B*-site cations													
Na	0.638	0.555	0.535	0.627	0.631	0.845	0.856	0.850	0.663	0.677	0.525	0.612	0.703
K											0.004		
Ca	1.253	1.296	1.238	1.233	0.177	1.146	1.123	1.104	1.117	1.143	1.261	1.269	1.216
Mn	0.009	0.012	0.014	0.004	0.009					0.004	0.015	0.012	0.007
Sr	0.016	0.004	0.004	0.015	0.013	0.017	0.026	0.017	0.011	0.004	0.014	0.008	0.011
Ba											0.002		0.002
Y	0.004		0.007	0.006	0.006				0.005	0.008	0.009	0.000	
La	0.009	0.009	0.012	0.011	0.015	0.011	0.007	0.010	0.018	0.015	0.017	0.012	0.006
Ce	0.042	0.038	0.059	0.049	0.069	0.042	0.024	0.039	0.096	0.089	0.107	0.069	0.041
Pr	0.002				0.004				0.004	0.004	0.004		
Nd	0.005	0.005	0.010	0.006	0.007	0.008	0.003	0.007	0.012	0.011	0.016	0.007	0.006
Sm				0.002					0.002	0.002		0.002	0.002
Pb	0.002							0.001			0.003		
Th	0.001	0.001				0.006	0.001	0.005	0.005	0.005	0.010	0.003	0.001
U	0.082	0.118	0.139	0.083	0.103	0.004	0.001	0.002	0.062	0.057	0.033	0.014	0.006
Total *A*	2.063	2.037	2.018	2.037	1.033	2.078	2.039	2.034	1.995	2.020	2.018	2.008	2.000
Nb	1.837	1.808	1.792	1.838	1.824	1.839	1.868	1.865	1.707	1.719	1.727	1.817	1.888
Ta										0.003			
Ti	0.005	0.003	0.007	0.007	0.006	0.004	0.015	0.005	0.012	0.016	0.004	0.004	0.005
Zr	0.001		0.004		0.002	0.098	0.069	0.072	0.164	0.148	0.147	0.042	0.014
Hf													
Fe	0.035	0.050	0.057	0.040	0.046	0.035	0.027	0.035	0.063	0.056	0.060	0.064	0.043
Mg	0.112	0.130	0.132	0.106	0.113	0.013	0.010	0.014	0.047	0.051	0.051	0.056	0.041
Al	0.007	0.005	0.005	0.006	0.005	0.004	0.002	0.003	0.005	0.003	0.006	0.007	0.005
Si	0.004	0.003	0.002	0.003	0.002	0.007	0.010	0.006	0.002	0.005	0.005	0.006	0.003
W		0.003			0.002							0.003	
Total *B*	2.000	2.000	2.000	2.000	2.000	2.000	2.000	2.000	2.000	2.000	2.000	2.000	2.000
F	0.781	0.785	0.605	0.711	0.710	0.924	0.920	0.947	0.745	0.745	0.705	0.803	0.899
OH_{calc}	0.509	0.523	0.728	0.556		0.241	0.159	0.139	0.398	0.434	0.600	0.364	0.226
$F+OH_{calc}$	1.291	1.308	1.333	1.267	0.710	1.165	1.079	1.086	1.143	1.179	1.305	1.167	1.125

Prepublished Article

O_{calc}	0.255	0.262	0.364	0.278		0.120	0.080	0.069	0.199	0.217	0.300	0.182	0.113
$F+O_{calc}$	1.036	1.046	0.969	0.989	0.710	1.045	1.000	1.017	0.944	0.962	1.005	0.985	1.012

Prepublished Article

Table 1. Continued.

Crystal	LL 444						LL 446						
Image	Fig. 4d												
Morphology	octahedral						octahedral						
Zonation	unzoned			unzoned		unzoned	oscillatory-type					irregular (alteration?)	
Position	angular cores			mantle		rim	core		mantle			rim	
Point	17	19	20	18	22	23	33	34	35	37	38	41	42
wt.%													
Na_2O	3.64	3.82	3.36	5.30	5.24	6.54	4.72	4.85	5.90	5.10	5.41	6.32	6.14
K_2O	0.05	0.08	0.07	0.06			0.07						
CaO	15.33	14.77	15.15	13.62	13.29	13.92	13.60	16.32	18.82	19.18	18.26	14.80	15.54
MnO							0.06	0.15		0.08	0.09		
SrO	0.08	0.17		0.09	0.11	0.29	0.29	0.26	0.31	0.46	0.31	0.24	0.31
BaO													
Y_2O_3		0.11	0.16					0.23	0.16	0.12	0.16		
La_2O_3	0.13	0.20	0.22	0.18	0.14	0.12	0.32	0.53	0.36	0.32	0.40	0.36	0.50
Ce_2O_3	1.31	1.14	1.32	0.95	0.91	0.86	1.99	3.43	1.69	1.60	1.99	2.01	2.33
Pr_2O_3			0.12					0.20				0.10	0.13
Nd_2O_3	0.24	0.19	0.11	0.19	0.09		0.33	0.39	0.15	0.22	0.22	0.24	0.29
Sm_2O_3			0.09			0.15	0.11			0.12			
PbO			0.08	0.16	0.21	0.11	0.15			0.09			0.07
ThO_2	0.35	0.38	0.27		0.09	0.22	0.24		0.08				0.06
UO_2	17.73	18.69	19.35	17.25	18.50	10.76	15.72	7.31		2.83	3.47	6.76	6.07
Nb_2O_5	41.45	41.08	38.15	48.61	47.36	58.28	51.38	58.69	64.00	62.09	62.27	62.37	62.51
Ta_2O_5	0.64	0.75	0.85	0.54	0.65	0.25	0.23			0.12		0.19	
TiO_2	4.15	3.93	4.17	5.17	5.69	1.93	0.33	0.64	2.55	1.14	1.09	0.56	0.67
ZrO_2	12.28	12.61	14.42	4.67	4.26	3.28	6.91	2.07	1.92	2.69	2.79	2.60	2.65
HfO_2		0.19	0.26										
Fe_2O_3	0.61	0.57	0.46	0.86	0.81	0.64	0.82	0.99	0.38	0.84	0.82	0.42	0.62
MgO	0.03	0.03		0.03	0.07	0.11	0.80	0.85	0.25	0.71	0.62	0.45	0.46
Al_2O_3	0.03	0.05	0.05	0.11	0.10	0.09	0.10	0.05	0.08	0.10	0.10	0.08	0.08
SiO_2	0.04	0.05	0.07	0.04		0.02	0.04	0.07		0.07	0.07	0.04	0.02
WO_3	0.16	0.26			0.17								
F	1.49	1.51	1.63	1.92	1.89	3.04	1.83	3.13	4.62	4.13	3.82	3.47	3.50
$-O=F_2$	0.63	0.64	0.69	0.81	0.80	1.28	0.77	1.32	1.95	1.74	1.61	1.46	1.47
Total	99.11	99.95	99.68	98.95	98.79	99.33	99.28	98.86	99.34	100.27	100.26	99.56	100.46

Structural formulae calculated on the basis of 2 *B*-site cations

Prepublished Article

Na	0.492	0.518	0.462	0.705	0.705	0.838	0.634	0.624	0.703	0.615	0.654	0.789	0.760
K	0.004	0.007	0.006	0.005			0.006						
Ca	1.147	1.107	1.151	1.001	0.988	0.986	1.009	1.159	1.239	1.278	1.221	1.020	1.063
Mn							0.003	0.009		0.004	0.005		
Sr	0.003	0.007		0.004	0.005	0.011	0.012	0.010	0.011	0.016	0.011	0.009	0.011
Ba													
Y		0.004	0.006					0.008	0.005	0.004	0.005		
La	0.003	0.005	0.006	0.005	0.004	0.003	0.008	0.013	0.008	0.007	0.009	0.009	0.012
Ce	0.033	0.029	0.034	0.024	0.023	0.021	0.051	0.083	0.038	0.036	0.045	0.047	0.054
Pr			0.003					0.005				0.002	0.003
Nd	0.006	0.005	0.003	0.005	0.002		0.008	0.009	0.003	0.005	0.005	0.006	0.007
Sm			0.002			0.003	0.003			0.003			
Pb			0.001	0.003	0.004	0.002	0.003			0.001			0.001
Th	0.006	0.006	0.004		0.001	0.003	0.004		0.001				0.001
U	0.275	0.291	0.305	0.263	0.286	0.158	0.242	0.108		0.039	0.048	0.097	0.086
Total *A*	1.970	1.980	1.985	2.013	2.017	2.026	1.982	2.028	2.009	2.009	2.004	1.979	1.998
Nb	1.308	1.299	1.223	1.507	1.486	1.742	1.608	1.759	1.778	1.746	1.756	1.815	1.804
Ta	0.012	0.014	0.016	0.010	0.012	0.004	0.004			0.002		0.003	
Ti	0.218	0.207	0.223	0.267	0.297	0.096	0.017	0.032	0.118	0.053	0.051	0.027	0.032
Zr	0.418	0.430	0.499	0.156	0.144	0.106	0.233	0.067	0.057	0.082	0.085	0.082	0.083
Hf		0.004	0.005										
Fe	0.032	0.030	0.025	0.044	0.042	0.032	0.043	0.050	0.018	0.040	0.039	0.021	0.030
Mg	0.003	0.003		0.004	0.007	0.011	0.083	0.084	0.023	0.066	0.057	0.043	0.044
Al	0.002	0.004	0.004	0.009	0.008	0.007	0.008	0.004	0.006	0.007	0.007	0.006	0.006
Si	0.003	0.004	0.005	0.003		0.002	0.003	0.005		0.005	0.005	0.003	0.001
W	0.003	0.005			0.003								
Total *B*	2.000	2.000	2.000	2.000	2.000	2.000	2.000	2.000	2.000	2.000	2.000	2.000	2.000
F	0.329	0.334	0.365	0.417	0.415	0.636	0.401	0.657	0.898	0.813	0.753	0.707	0.706
OH_{calc}	1.006	1.018	1.022	0.917	0.957	0.614	0.881	0.648	0.182	0.294	0.356	0.425	0.460
$F+OH_{calc}$	1.335	1.353	1.388	1.334	1.372	1.250	1.281	1.305	1.080	1.108	1.109	1.132	1.166
O_{calc}	0.503	0.509	0.511	0.458	0.479	0.307	0.440	0.324	0.091	0.147	0.178	0.212	0.230
$F+O_{calc}$	0.832	0.844	0.876	0.876	0.893	0.943	0.841	0.981	0.989	0.960	0.931	0.919	0.936

Republished Article

Table 1. Continued.

Crystal	KZ 21									KZ 24							
Image	Fig. 5a									Fig. 5b							
Morphology	cubo-octahedral									octahedral							
Zonation	sector- and oscillatory-type									sector-type				oscillatory-type			
Position	core to rim - {100}					core to rim - {111}				core - {100}		core - {111}		mantle		rim	
Point	11	19	20	21	23	14	15	16	17	24	26	25	27	30	36	37	41
wt.%																	
Na_2O	5.98	5.82	5.94	5.87	5.79	6.37	6.24	6.18	6.12	5.21	5.34	5.68	5.62	5.61	5.48	5.64	5.69
K_2O				0.07	0.05	0.07	0.08		0.05	0.07		0.11	0.06	0.05	0.06	0.06	0.05
CaO	19.68	19.62	19.72	19.42	19.95	18.30	18.55	18.58	18.67	19.11	19.40	17.13	18.39	19.50	19.18	19.09	19.55
MnO																	
SrO	0.56	0.66	0.56	0.57	0.63	0.58	0.71	0.51	0.37	0.43	0.24	0.31	0.36	0.33	0.43	0.56	0.23
BaO																	
Y_2O_3		0.12			0.11							0.11					0.15
La_2O_3				0.06				0.08			0.07					0.05	
Ce_2O_3	0.11	0.14				0.14	0.13	0.11	0.13	0.18	0.14	0.20	0.11		0.12	0.18	0.21
Pr_2O_3																	
Nd_2O_3	0.12																
Sm_2O_3										0.10					0.08		
PbO			0.12	0.06					0.20	0.08					0.10	0.16	0.12
ThO_2						0.05											
UO_2	0.81	0.84	0.39	0.59	0.54	2.97	2.68	2.71	2.94	5.87	5.08	8.82	6.52	3.20	4.00	2.54	1.51
Nb_2O_5	64.25	63.88	62.76	63.95	63.49	62.07	60.62	62.39	61.36	57.72	57.72	55.04	56.09	60.91	61.03	61.11	59.29
Ta_2O_5								0.14			0.25		0.15	0.15			
TiO_2	4.23	3.65	5.22	4.21	4.91	4.22	5.19	4.92	5.12	5.20	5.25	5.16	7.00	4.92	4.53	4.21	7.02
ZrO_2		0.14	0.15	0.17		0.16				1.73	1.81	1.24	0.24	0.97	0.86	0.24	
HfO_2																	
Fe_2O_3	1.25	1.59	0.80	1.10	0.84	1.48	1.00	1.08	1.15	1.56	1.51	1.58	1.02	1.31	1.61	1.72	0.61
MgO				0.03								0.04				0.04	
Al_2O_3	0.03									0.03							
SiO_2	0.02	0.06	0.04	0.03	0.05	1.04	0.90	0.40	0.59	0.16	0.05	0.87	0.72		0.02	0.07	0.06
WO_3										0.16		0.14			0.20		
F	5.17	4.87	5.04	4.70	4.58	4.69	4.45	4.95	4.78	4.31	4.34	3.28	4.09	4.29	4.58	4.50	4.84
$-O=F_2$	2.18	2.05	2.12	1.98	1.93	1.98	1.87	2.09	2.01	1.82	1.83	1.38	1.72	1.81	1.93	1.90	2.04
Total	100.03	99.34	98.62	98.83	99.00	100.17	98.65	99.96	99.45	100.10	99.37	98.33	98.65	99.42	100.34	98.29	97.29

Structural formulae calculated on the basis of 2 *B*-site cations

Prepublished Article

Na	0.698	0.685	0.698	0.688	0.679	0.738	0.734	0.723	0.718	0.626	0.643	0.699	0.675	0.665	0.650	0.677	0.677
K				0.005	0.003	0.005	0.006		0.004	0.005		0.008	0.005	0.004	0.005	0.005	0.004
Ca	1.270	1.276	1.280	1.259	1.293	1.172	1.206	1.201	1.211	1.269	1.292	1.165	1.221	1.276	1.257	1.265	1.285
Mn																	
Sr	0.019	0.023	0.020	0.020	0.022	0.020	0.025	0.018	0.013	0.016	0.009	0.011	0.013	0.012	0.015	0.020	0.008
Ba																	
Y		0.004			0.004							0.004					0.005
La				0.001				0.002			0.002					0.001	
Ce	0.003	0.003				0.003	0.003	0.002	0.003	0.004	0.003	0.005	0.003		0.003	0.004	0.005
Pr																	
Nd	0.003																
Sm										0.002					0.002		
Pb			0.002	0.001					0.003	0.001					0.002	0.003	0.002
Th						0.001											
U	0.011	0.011	0.005	0.008	0.007	0.040	0.036	0.036	0.040	0.081	0.070	0.125	0.090	0.043	0.054	0.035	0.021
Total *A*	2.003	2.003	2.005	1.982	2.008	1.978	2.009	1.982	1.991	2.004	2.019	2.017	2.007	2.000	1.987	2.009	2.006
Nb	1.749	1.753	1.719	1.749	1.736	1.677	1.663	1.701	1.679	1.618	1.622	1.579	1.572	1.682	1.687	1.709	1.644
Ta								0.002			0.004		0.002	0.002			
Ti	0.192	0.167	0.238	0.192	0.223	0.190	0.237	0.223	0.233	0.242	0.246	0.246	0.327	0.226	0.208	0.196	0.324
Zr		0.004	0.004	0.005		0.005				0.052	0.055	0.038	0.007	0.029	0.025	0.007	
Hf																	
Fe	0.057	0.073	0.036	0.050	0.038	0.067	0.046	0.049	0.052	0.073	0.070	0.076	0.047	0.060	0.074	0.080	0.028
Mg				0.002								0.003	0.000			0.003	
Al	0.002									0.002							
Si	0.001	0.004	0.002	0.002	0.003	0.062	0.055	0.024	0.036	0.010	0.003	0.055	0.044		0.001	0.005	0.004
W										0.003		0.002			0.003		
Total *B*	2.000	2.000	2.000	2.000	2.000	2.000	2.000	2.000	2.000	2.000	2.000	2.000	2.000	2.000	2.000	2.000	2.000
F	0.985	0.935	0.966	0.900	0.876	0.887	0.853	0.945	0.915	0.846	0.854	0.658	0.801	0.829	0.885	0.881	0.939
OHcalc	0.040	0.095	0.038	0.083	0.173	0.021	0.118	0.027	0.054	0.248	0.242	0.427	0.241	0.214	0.166	0.153	0.060
F+OHcalc	1.025	1.030	1.004	0.983	1.049	0.907	0.971	0.972	0.969	1.094	1.096	1.084	1.043	1.043	1.051	1.034	0.999
Ocalc	0.020	0.047	0.019	0.042	0.086	0.010	0.059	0.014	0.027	0.124	0.121	0.213	0.121	0.107	0.083	0.076	0.030
F+Ocalc	1.005	0.983	0.985	0.941	0.963	0.897	0.912	0.958	0.942	0.970	0.975	0.871	0.922	0.936	0.968	0.957	0.969

Prepublished Article

Table 1. Continued.

Crystal	KZ 22						KZ 23				
Image	Fig. 5c						Fig. 5d				
Morphology	unknown (crystal fragment)						cubo-octahedral				
Zonation	sector- and oscillatory type						oscillatory-type				
Position	core to rim – {100}?			core to rim - {111}?			core	core	mantle	mantle	rim
Point	50	51	52	45	47	49	53	55	57	59	6
wt.%											
Na_2O	5.59	5.77	5.67	5.96	6.10	6.15	6.56	6.35	6.81	6.66	7.02
K_2O	0.07		0.08	0.09	0.08	0.08	0.12	0.09	0.08		0.05
CaO	19.36	19.78	19.66	17.27	18.01	18.36	18.73	18.57	16.52	16.80	18.75
MnO					0.07						
SrO	0.33	0.36	0.43	0.44	0.46	0.53	0.61	0.44	0.51	0.40	0.74
BaO						0.15					0.16
Y_2O_3								0.10			
La_2O_3	0.08	0.05		0.07	0.09	0.06			0.05	0.05	
Ce_2O_3	0.23	0.27	0.17	0.37	0.29	0.20			0.24	0.12	
Pr_2O_3											
Nd_2O_3											
Sm_2O_3											
PbO				0.08	0.14	0.10	0.17			0.07	0.06
ThO_2	0.05		0.08	0.12	0.15	0.09	0.11		0.09	0.11	0.05
UO_2	2.76	0.89	1.51	5.65	3.02	2.95	2.13	2.71	3.00	3.66	0.96
Nb_2O_5	60.56	62.04	61.40	57.94	59.54	60.40	56.92	58.61	65.68	63.18	60.30
Ta_2O_5			0.18	0.34	0.14	0.14					
TiO_2	4.58	4.23	4.38	4.66	4.20	4.31	6.72	5.81	1.71	2.41	7.30
ZrO_2	0.34		0.15	0.32	0.13	0.18	0.87	0.86			0.12
HfO_2											
Fe_2O_3	1.72	1.64	1.78	1.84	1.64	1.64	0.80	0.85	1.38	1.48	0.33
MgO											
Al_2O_3			0.03								0.03
SiO_2	0.05	0.04	0.07	0.89	0.87	0.88	2.28	1.40	0.09	0.30	0.82
WO_3		0.15									0.49
F	4.47	4.96	5.00	3.82	4.66	4.61	4.79	4.60	4.55	4.55	5.06
$-O=F_2$	1.88	2.09	2.10	1.61	1.96	1.94	2.02	1.94	1.92	1.92	2.13
Total	98.30	98.09	98.47	98.25	97.61	98.74	98.76	98.45	98.78	97.86	100.08

Structural formulae calculated on the basis of 2 *B*-site cations

Prepublished Article

Na	0.670	0.687	0.674	0.717	0.733	0.727	0.747	0.738	0.823	0.812	0.799
K	0.005		0.006	0.007	0.006	0.006	0.009	0.007	0.006		0.003
Ca	1.283	1.302	1.291	1.149	1.196	1.200	1.178	1.194	1.103	1.133	1.180
Mn					0.003						
Sr	0.012	0.013	0.015	0.016	0.016	0.019	0.021	0.015	0.018	0.014	0.025
Ba						0.004					0.004
Y								0.003			
La	0.002	0.001		0.002	0.002	0.001			0.001	0.001	
Ce	0.005	0.006	0.004	0.008	0.007	0.005			0.005	0.003	
Pr											
Nd											
Sm											
Pb				0.001	0.002	0.002	0.003			0.001	0.001
Th	0.001		0.001	0.002	0.002	0.001	0.001		0.001	0.002	0.001
U	0.038	0.012	0.021	0.078	0.042	0.040	0.028	0.036	0.042	0.051	0.012
Total *A*	2.015	2.021	2.012	1.980	2.009	2.005	1.985	1.994	1.999	2.017	2.026
Nb	1.693	1.724	1.702	1.626	1.668	1.665	1.510	1.590	1.849	1.797	1.602
Ta			0.003	0.006	0.002	0.002					
Ti	0.213	0.196	0.202	0.217	0.196	0.198	0.297	0.262	0.080	0.114	0.323
Zr	0.010		0.005	0.010	0.004	0.005	0.025	0.025			0.003
Hf											
Fe	0.080	0.076	0.082	0.086	0.077	0.075	0.035	0.039	0.065	0.070	0.014
Mg											
Al			0.002								0.002
Si	0.003	0.003	0.004	0.055	0.054	0.054	0.134	0.084	0.006	0.019	0.048
W		0.002									0.007
Total *B*	2.000	2.000	2.000	2.000	2.000	2.000	2.000	2.000	2.000	2.000	2.000
F	0.874	0.964	0.969	0.750	0.914	0.889	0.888	0.874	0.897	0.906	0.940
OH_{calc}	0.178	0.075	0.043	0.201	0.055	0.068			0.149	0.153	
$F+OH_{calc}$	1.053	1.039	1.011	0.951	0.969	0.957	0.888	0.874	1.046	1.059	0.940
O_{calc}	0.089	0.038	0.021	0.100	0.027	0.034			0.075	0.077	
$F+O_{calc}$	0.963	1.002	0.990	0.851	0.941	0.923	0.888	0.874	0.972	0.982	0.940

Blanks in the Table – content of the element is below detection limit. OH_{calc} and O_{calc} – calculated from charge balance.

Republished Article

Table 2. Crystal data and structure refinement parameters.

Sample	LL 441	KS 23
Crystal data		
Ideal formula	$Ca_{1.86}U_{0.14}Nb_{1.86}O_6F$	$Ca_{1.36}Na_{0.65}Nb_{1.85}O_6F$
Crystal dimensions (mm)	0.22 x 0.17 x 0.14	0.24 x 0.18 x 0.12
Crystal system, space group	Cubic, $Fd\bar{3}m$	Cubic, $Fd\bar{3}m$
a (Å)	10.434(4)	10.398(2)
V (Å^3)	1135.9(14)	1124.1(6)
Z	8	8
Calculated density (g cm^3)	4.622	4.205
μ (mm^{-1})	9.315	5.062
Data collection		
Crystal description	octahedral	cubo-octahedral
Instrument	STOE IPDS II	STOE IPDS II
Radiation type, wavelength (Å)	Mo-$K\alpha$, 0.71073	Mo-$K\alpha$, 0.71073
F(000)	1465.0	1336.0
θ (°)	3.382 to 29.108	3.394 to 36.017
Absorption correction	Multifaceted crystal, XShape	Multifaceted crystal, XShape
No. of measured, independent and observed [$I > 2\sigma(I)$] reflections	2493, 97, 90	4721, 155, 139
R_{int}	0.0560	0.0262
Data completeness (%)	100	97
Indices range of h, k, l	$-12 \le h \le 14$, $-14 \le k \le 14$, $-14 \le l \le 14$	$-16 \le h \le 16$, $-16 \le k \le 16$, $-15 \le l \le 16$
Refinement		
Refinement	Full-matrix least squares on F^2	Full-matrix least squares on F^2
Number of reflections, parameters, restraints	97, 13, 0	155, 13, 0
R_1 [$I > 2\sigma(I)$], R_1(all)	0.0192, 0.0206	0.0119, 0.0290

Prepublished Article

wR_2 [$I > 2\sigma(I)$], wR_2 (all)	0.0378, 0.0383	0.0140, 0.0294
GoF	1.272	1.178
No. of refined parameters	13	13
$\Delta\rho_{max}/\Delta\rho_{min}$ (e^- Å^{-3})	0.52/-0.30	0.27/-0.27

Table 3. Atom coordinates, equivalent displacement parameters (Å^2) and site occupancies.

Sample	site	*x/a*	*y/b*	*z/c*	*U*eq	Occupancy	Refined occupancy	s.s.[1] (epfu)	s.s.$_{calc}$[1] (epfu)
LL 441	*A*	1	½	0	0.0143(7)	$Ca_{0.515}Na_{0.325}U_{0.08}$ $Ce_{0.06}La_{0.01}Nd_{0.01}$ $Pr_{0.005}Mn_{0.005}$ $Sr_{0.005}Y_{0.005}$	$Ca_{0.932(4)}$ $U_{0.068(4)}$	25.0	26.4
KS 23	*A*	1	½	0	0.0149(4)	$Ca_{0.58}Na_{0.39}U_{0.015}$ $Sr_{0.01}$	$Ca_{0.677(2)}$ $Na_{0.323(2)}$	17.1	17.7
LL 441	*B*	¾	½	¼	0.0118(4)	$Nb_{0.865}Zr_{0.06}Mg_{0.04}$ $Fe_{0.035}Al_{0.005}$	$Nb_{0.93(1)}$	38.1	39.3
KS 23	*B*	¾	½	¼	0.0118(1)	$Nb_{0.835}Ti_{0.11}Si_{0.03}$ $Fe_{0.02}Zr_{0.005}$	$Nb_{0.924(6)}$	37.7	37.8
LL 441	O^2	0.8210(3)	⅝	⅛	0.0159(9)	O	O	8.0	8.0
KS 23	O^2	0.8196(1)	⅝	⅛	0.0130(3)	$O_{0.98}OH_{0.02}$	O	8.0	8.0
LL 441	Z^2	⅛	⅝	⅛	0.026(2)	$F_{0.54}O_{0.46}$	F	9.0	8.5
KS 23	Z^2	⅛	⅝	⅛	0.0146(5)	$F_{0.90}OH_{0.10}$	F	9.0	8.9

[1] – s.s. – refined site scattering; s.s.$_{calc}$ – calculated site scattering
[2] - O/OH/F ratio in O and *Z* sites is calculated from the charge balance of formulas and amount of F.

Prepublished Article

Table 4. Selected interatomic distances (Å).

LL 441		KS 23	
A - O	2.625(3) x6	*A* - O	2.626 (1) x6
A - *Z*	2.2590(9) x2	*A* - *Z*	2.2511(4) x2
<*A* - O,*Z*>	2.534	<*A* - O,*Z*>	2.532
B - O	1.988(2) x6	*B* - O	1.9752 (6) x6

Table 5. Sector zoning in pyrochlore crystals.

Data source	This study			Hodgson and Le Bas (1992)		
Sample	KS 21	KS 24	KS 22	A	B	C
A site						
Na	0.041 / 0.708	0.033 / 0.671	0.047 / 0.702	0.018 / 0.653	0.050 / 0.622	0.079 / 0.634
K	0.001 / 0.004	0.001 / 0.005	0.002 / 0.006	-0.0004 / 0.0008	-0.0004 / 0.0007	-0.0002 / 0.0007
Ca	-0.080 / 1.237	-0.091 / 1.239	-0.120 / 1.232	-0.063 / 1.186	-0.101 / 1.242	-0.115 / 1.221
Sr	-0.002 / 0.020	0.002 / 0.011	0.004 / 0.014	-0.003 / 0.013	-0.007 / 0.015	-0.005 / 0.014
Pb	bdl	bdl	bdl	0.002 / 0.005	0.0001 / 0.005	0.003 / 0.004
Ce	0.000 / 0.002	0.002 / 0.004	0.002 / 0.007	-0.001 / 0.005	-0.002 / 0.006	-0.002 / 0.006
La	bdl	bdl	bdl	-0.0002 / 0.001	-0.0003 / 0.002	-0.0005 / 0.001
U	0.030 / 0.023	0.051 / 0.082	0.035 / 0.043	0.046 / 0.161	0.049 / 0.135	0.036 / 0.145
B site						
Nb	-0.059 / 1.710	-0.077 / 1.614	-0.062 / 1.678	-0.021 / 1.464	-0.003 / 1.476	0.034 / 1.488
Ti	0.016 / 0.213	0.051 / 0.261	0.002 / 0.206	0.124 / 0.317	0.154 / 0.275	0.146 / 0.276
Zr	0.001 / 0.005	-0.020 / 0.032	0.000 / 0.010	-0.103 / 0.218	-0.149 / 0.250	-0.181 / 0.237
Fe	0.004 / 0.051	0.003 / 0.063	0.004 / 0.080	0.001 / 0.003	0.002 / 0.002	0.002 / 0.002
Si	0.042 / 0.024	0.052 / 0.029	0.052 / 0.029	0.046 / 0.037	0.043 / 0.023	0.034 / 0.025

First number in each cell denotes the difference $\Delta x = x_{\{111\}} - x_{\{100\}}$, apfu, and the second one – the average value $x_{av} = (x_{\{111\}} + x_{\{100\}}) / 2$, apfu, respectively (calculated on the basis of two *B*-site cations). Sample KS 21 – values averaged over 4 pairs of points, sample KS 24 – over 2 pairs of points (Table 1, Supplementary Figure 1). bdl – below detection limit. * For the sample KS 22 no morphological observations were possible and {*hkl*} indices were ascribed to growth sectors using the concentration differences in U.

Preprint Article

Table 6. Fractal dimension of strange attractor D_{max} for pyrchlore crystals.

Sample	Fig.	Profile length, μm	Number of points in profile	D_{max}
LL 445	4a, 10a	42	500	2.8(1)
LL 447	4c, 10b	49	341	2.7(2)
KS 24	5b, 10c	45	285	3.2(1)
Hogarth *et al*. (2000)	10d	275	257	2.9(1)
Ru; Kovdor (this study)	-	47	366	2.7 / 3.0*
Ld; Kovdor (this study)	-	98	519	2.5 / 3.8*

*Two values of D_{max} reflect presence of two saturation values on $D(D_{emb})$ plots.

Prepublished Article